

CONSTRAINING THE HIGH DENSITY NUCLEAR SYMMETRY ENERGY WITH PIONS

By

Justin Estee

A DISSERTATION

Submitted
to Michigan State University
in partial fulfillment of the requirements
for the degree of

Physics – Doctor of Philosophy

2019

ABSTRACT

CONSTRAINING THE HIGH DENSITY NUCLEAR SYMMETRY ENERGY WITH PIONS

By

Justin Estee

Copyright by
JUSTIN ESTEE
2019

ACKNOWLEDGEMENTS

Your acknowledgements here.

TABLE OF CONTENTS

LIST OF TABLES	vi
LIST OF FIGURES	vii
CHAPTER 1 DATA ANALYSIS I: CALIBRATION AND CORRECTIONS	1
1.1 Software	1
1.1.1 Pulse Shape Algorithm	4
1.2 Calibrations and Corrections	4
1.2.1 Gating grid noise subtraction	4
1.2.2 Cocktail calibration	5
1.2.3 Electronics calibration	8
1.2.4 Anode gain calibration	9
1.2.5 Extending the dynamic range of the Electronics	10
1.2.6 Experimental Pad Response Function	13
1.2.7 Method of Desaturation	14
1.2.8 Space Charge Corrections	18
1.3 Monte Carlo Simulation	26
1.3.1 Drift Task	29
1.3.2 Pad Response Task	31
1.3.3 Electronics Task	31
1.3.4 Simulating Saturation	33
1.4 Monte Carlo Track Embedding	37
1.4.1 MC and Data Comparison	42
1.5 Aligning TPC	43
1.6 CoBo timing correction	43
1.7 Efficiency Corrections	44
APPENDIX	46
BIBLIOGRAPHY	49

LIST OF TABLES

Table 1.1	Summary of expected cocktail.	6
Table 1.2	Summary of expected cocktail.	6
Table 1.3	Summary of expected cocktail.	6
Table 1.4	Summary of expected cocktail.	8
Table 1.5	An overview of the properties of the TPC	29
Table .1	List of runs for the analysis.	47

LIST OF FIGURES

Figure 1.1	Cartoon graphic of a top down view of a fit to a track passing through several pads. The bolded pads and the charges q_i represent the hits belonging to that pad and the clusters of the track representing the average position of the track. The three clusters at the bottom are clustered in the x-direction and for the upper three clustered in the z-direction. The estimate of the position of the avalanche is given by the track fit and the position from the center to each pad to the \bar{x} position is given as λ_i	3
Figure 1.2	Gating grid noise profile and subtraction for a particular pad.	5
Figure 1.3	Calibration of electronics	8
Figure 1.4	Calibration of low high.	9
Figure 1.5	The expected dE/dx lines of different particles are given in red as calculated by Geant4. The approximate dynamic range of the TPC is shown by the vertical bar for the gain setting used in the experiment. Anything outside of this region would be saturated to some degree.	12
Figure 1.6	PRF response from π^- data.	14
Figure 1.7	Parameters N_0 and σ as a function of the crossing angle θ with the 4 th order polynomial fits.	15
Figure 1.8	A typical case of a saturating event. The red pulses represent the time bucket signal for each collected charge. The pads directly underneath the avalanche point, $q_{2'}$ and $q_{3'}$, are saturated while pads farther away, q_1 and q_4 are not saturated.	16
Figure 1.9	Uncorrected (left panel) and desaturated (right panel) collision data at polar angles of $\theta < 40^\circ$ and azimuthal angles between $-80^\circ < \phi < 80^\circ$	17
Figure 1.10	Location of space charge in ^{132}Sn	19
Figure 1.11	Beam path of the experiments	20
Figure 1.13	ΔV_x distribution for left-going and right-going tracks in the TPC for the	22
Figure 1.12	Shift of tracks	23
Figure 1.14	ΔV_{LR} versus the beam rate for all systems with the fitted function.	24

Figure 1.15 Space charge fit function versus the beam rate for all systems. These are the assumed functions we use for interpolating the space charge value from the beam rate.	25
Figure 1.16 Space charge relation	26
Figure 1.17 Distribution of estimated space charge densities for each beam type.	27
Figure 1.18 Residuals in the fitted line of ΔV_{LR} observable for all systems.	27
Figure 1.20 PRF response of Monte Carlo simulation of π^-	32
Figure 1.21 Standard pulse	33
Figure 1.22 Pole zero correction	34
Figure 1.23 Geant4 simulation of ^{108}Sn beam at 270 MeV/A in P10 gas. Notice the extent of the delta electrons in the vertical direction as compared to the horizontal extent.	35
Figure 1.24 Tagging the saturated pads.	36
Figure 1.25 Flow of embedding implementation in the software.	39
Figure 1.26 A 200 MeV/c π^- embedded into a nuclear collision type event. The embedded track identified by the software is highlighted by the solid green line.	39
Figure 1.27 A 200 MeV/c π^- embedded into a nuclear collision type event. The embedded track identified by the software is highlighted by the solid green line.	40
Figure 1.28 Comparison of MC to data.	42
Figure 1.29 Comparison of MC to data.	43
Figure 1.30 TBW	44
Figure 1.31	45

CHAPTER 1

DATA ANALYSIS I: CALIBRATION AND CORRECTIONS

Need to explain pedestal subtraction

1.1 Software

The S π RITROOT software is modular task based code based on the FAIRROOT package written in C++ [1]. The main tasks in the S π RITROOT software reconstruction are:

- Decoder task
- Pulse Shape Algorithm (PSA Task)
- Helix Track Finding Algorithm
- Clustering Algorithm
- Track Fitting (GENFIT package)
- Vertex Fitting (RAVE package)

The decoder task converts the binary data file into a container class which maps the electronics channels into the corresponding pads and (x,z) coordinates.

There may be several pulses in a pad coming from two tracks passing under the same pad separated by arrival time. Using an expected pulse shape the PSA task fits the signal pulses within a pad, giving the arrival time of the drifted electrons from each particular track. The height of the fitted pulse is proportional to the total charge of that event, Q and the y-coordinate is calculated as $y = v \cdot t_0$ where v is the drift velocity and t_0 the arrival time. Combining the information from these first two tasks, (x,y,z,Q), we construct what is called a "hit".

The Helix Track Finding Algorithm finds the collection of hits belonging to one track out of all the hits in an event. The hits within a track are then reduced into clusters. A cluster's position is

the average position of the hits within a cluster, with the total charge of the cluster being the sum of the hits charges.

A tracks average position is estimated by the cluster's average position. The clusters are then fitted in the GENFIT track fitting package [2], giving the final momentum of the track. A final vertex of the event is fitted from all tracks using the package RAVE [3].

Definition of clustering A brief description of the method of clustering is illustrated in Figure 1.1. It is impractical to cluster in both the x and z-axis and we only cluster the hits along one axis. The three clusters at the bottom of Figure 1.1 are clustered along the x-axis and the upper three are along the z-axis, as shown by the bolded pads for one of the clusters in each direction.

The clustering direction depends on the angle of the track with respects to the x-axis, defined as θ . For example, a track going along the z-axis the crossing angle is defined as 90° , and a track going along the x-axis defined as 0° . In the case that the crossing angle is $45^\circ < \theta \leq 90^\circ$ the clustering direction is along the x-axis. For $0^\circ < \theta \leq 45^\circ$ it is along the z-axis.

The position along the clustering direction is calculated by weighting the individual hit's positions by their charges q_i and getting the mean value. The other direction is set to the center of the pad. For example if we are clustering along the x-axis for a cluster, the z-position is set to the center of the pad in the z-direction and vice versa.

Clustering in this way gives us better position resolution for calculating the position of each cluster. You could imagine if we calculated the clusters only along the x-axis for tracks with $\theta \approx 0^\circ$ the x-position is not well defined. By clustering in the direction most perpendicular to the track, we get a better position resolution.

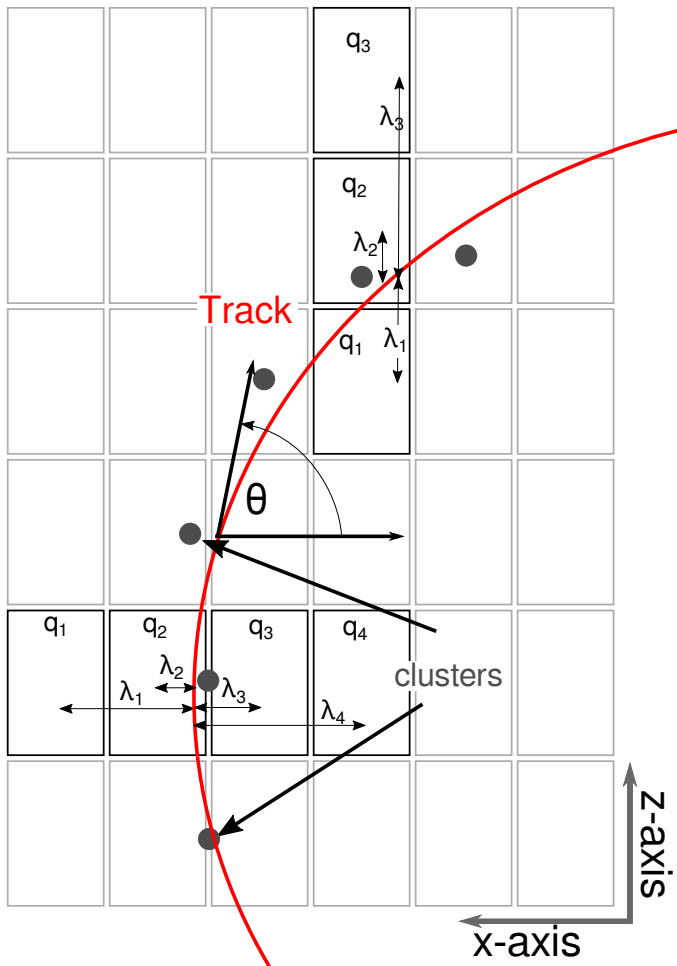


Figure 1.1: Cartoon graphic of a top down view of a fit to a track passing through several pads. The bolded pads and the charges q_i represent the hits belonging to that pad and the clusters of the track representing the average position of the track. The three clusters at the bottom are clustered in the x-direction and for the upper three clustered in the z-direction. The estimate of the position of the avalanche is given by the track fit and the position from the center to each pad to the \bar{x} position is given as λ_i .

1.1.1 Pulse Shape Algorithm

1.2 Calibrations and Corrections

1.2.1 Gating grid noise subtraction

Opening the gating grid essentially short adjacent wires together allowing them to reach equilibrium as fast as possible. In practice the impedance of both sides was not entirely matched properly and this caused an oscillating current to bounce back and forth in an under-dampened manner. This caused residual induced signals early in the time bucket spectrum which created an extra source of noise in the data. The ground grid shielded some of the noise, but the path to ground was on two ends and was not sufficient for this frequency. Figure 1.2 shows in the upper panel the gating grid noise ADC time bucket spectrum for 2000 events in a given pad. The signal is stable within a pad and the mean value –shown as the red line– can be calculated after averaging over several thousands events. The raw gating grid noise lasts for 100 tbs extending into the real data with a decreasing amplitude.

The gating grid itself was not always stable and only the ^{132}Sn and ^{124}Sn beams were relatively stable. Several times during the ^{108}Sn and ^{112}Sn beams the gating grid broke. After several data runs were taken, we took what is called gating grid noise runs to get the profile of the gating grid noise throughout the experiment. To achieve this the anode wires would be turned off and the trigger was allowed to otherwise operate normally, firing the gating grid to open as usual. Since the anode wires were all turned off no signals would be seen except those coming from the gating grid noise. Several thousand triggers of the gating grid were taken to get a good noise profile.

Once the mean value response in each pad is calculated, we can use the gating grid noise profile runs to correct the real data and remove the noise of the gating grid. To show the best case scenario of this technique, the bottom panel of Fig. 1.2 shows the gating grid noise self correcting itself. We can see the pedestal is already subtracted naturally when using this technique, and the subtracted ADC spectra is centered around 0. Residual gating grid noise that was not canceled

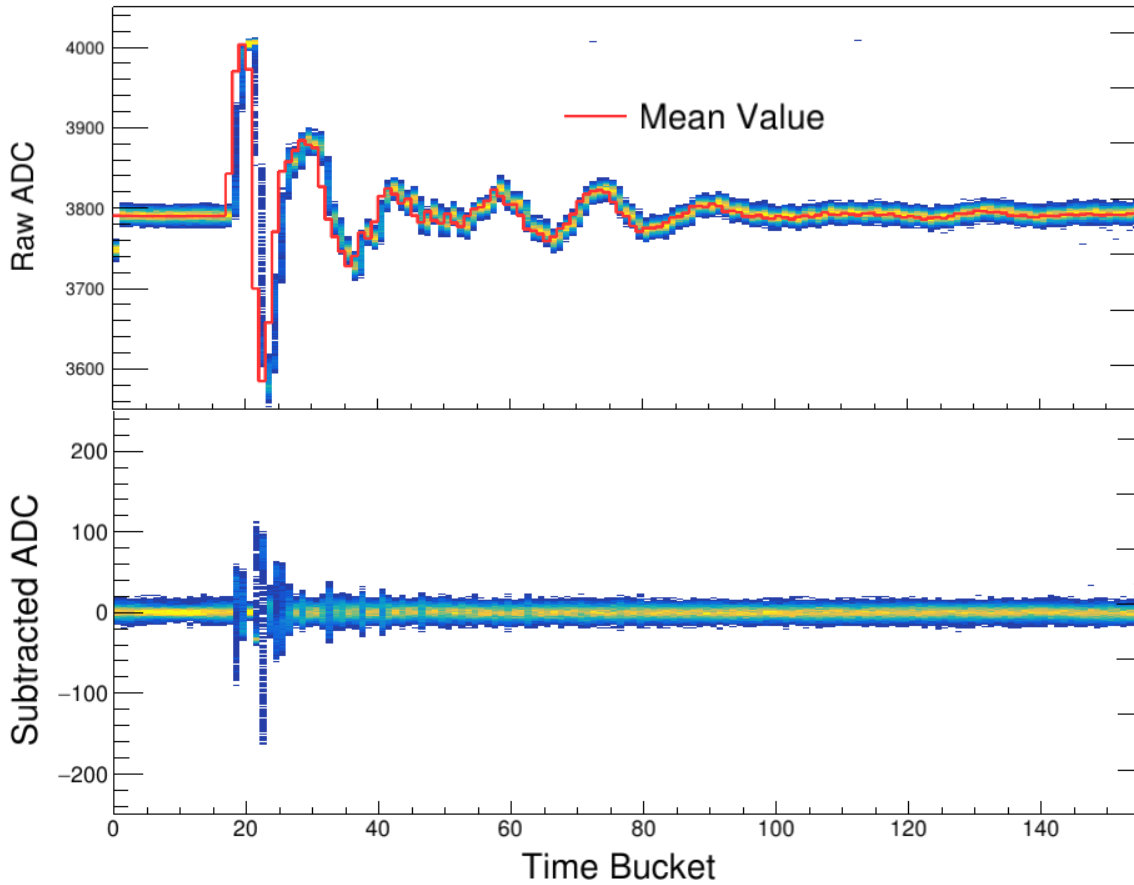


Figure 1.2: Gating grid noise profile and subtraction for a particular pad.

by the subtraction remains but is significantly reduced to a much smaller time bucket region. This happens in regions where the gating grid noise is changing rapidly, where the ADC value is dependent upon small jitters in the timing of the signal. All time buckets below 30 tb were cut away from the spectrum to get rid of the small region where the gating grid is still opening and to remove the residual noise.

1.2.2 Cocktail calibration

A cocktail of several light charged particles were produced ($p, d, t, {}^3\text{He}, {}^4\text{He}$), and measured in the TPC to provide a momentum calibration of the TPC. The magnetic and slit settings of the dipoles in the BIGRIPS spectrometer was set so that the measured momentum resolution of the beam

100MeV Target					
Particle	Measured	Corrected	% Difference	% Difference	
p	882.8	929.5	877.3	3.7	-1.0
d	817.1	831.15	797.94	1.7	-2.3

Table 1.1: Summary of expected cocktail.

100MeV					
Particle	Expected	Measured	Corrected	% Difference	% Difference
p	882.8	903.5	889	2.0	-1.6
d	817.1	898.5	874.5	2.1	-2.7

Table 1.2: Summary of expected cocktail.

300MeV						
Particle	Expected	Measured	Corrected	% Difference Raw	% Difference	Corrected
d	1621	1704	1612	5.1	-0.6	
t	1612	1691	1596	4.9	-1.0	
⁴ He	1613	1698	5.3	1595	-1.1	

Table 1.3: Summary of expected cocktail.

was $\delta p/p < 1\%$. Two magnetic rigidity settings were studied, with an empty target. A thick Aluminum target was used to provide a slightly lower energy point for part of the lower rigidity setting, effectively creating three calibration points over several particle species. The production of certain particles ($t, {}^3\text{He}$), produced too few counts to make a good measurement, and in the high momentum rigidity setting protons could not propagate down the line and there were no counts.

Since the expected momentum resolution resulting from the spectrometer was less than 1%, the observed momentum resolution measured by the TPC is a good representation of the combined momentum resolution of the software and TPC (intrinsic detection) system. The momentum resolution depends on several factors such as the particle's angle, momentum, charge, track multiplicity, etc.

This calibration beam represents an ideal situation where the track was parallel to the pad plane and only one particle was measured at one time. The energy loss resolution can also be directly measured since each energy setting represents a monochromatic source of each particle species, which has a well defined energy loss distribution. An average momentum resolution of $dp/p = 2\%$ and the energy loss resolution of $d\langle dE/dx \rangle / \langle dE/dx \rangle = 5\%$ was measured for particles ranging from H to ${}^4\text{He}$, over the range of momenta measured in the calibration beam as summarized in Table 1.4.

Since the magnetic dipole setting of the BIGRIPS spectrometer defined the energy of each particle type, we can calculate the expected momenta of each particle species measured. Small corrections were propagated using LISE++ software which can calculate the energy loss through several materials in the beam line. These corrections resulted in a small change in the momenta. The measured momenta of the calibration beam differed significantly from the expected values as seen in Tables tables 1.1 to 1.3. This effect is attributed to inhomogeneities in the magnetic field which introduces electron drift velocity in the direction of $\vec{E} \times \vec{B}$ direction as seen from Eq.???. The $\vec{E} \times \vec{B}$ drift velocity causes the electron trajectories to shift toward the $+x$ -axis in the TPC coordinates causing particles of positive charge (going in the $-x$ -axis) to have a higher measured momenta than in reality. The disagreement in measured and expected momenta is upwards of 5% difference in the higher momentum calibration settings. The details of the correcting for the $\vec{E} \times \vec{B}$ effect will be discussed in the later Section 1.2.8 in a more general way which also includes correction for the space charge, which this cocktail beam does not have. The same correction technique was applied here in the special case of zero space charge, which is the special case of only having $\vec{E} \times \vec{B}$ components.

The values under the corrected column seen in Tables tables 1.1 to 1.3, represent the data corrected for the $\vec{E} \times \vec{B}$ effect. A significant improvement is seen in the high momentum setting going from around 5% disagreement to within 1% agreement in the corrected data. For the lower momentum settings (Tables tables 1.1 and 1.2), protons see a slight improvement of about 1% where as the deuterons are over corrected in both settings. The level of agreement of the all

Momentum Resolution %	$\langle dE/dx \rangle$ Resolution %
1.6	4.6

Table 1.4: Summary of expected cocktail.

corrected values is still within the estimated momentum resolution of the TPC.

1.2.3 Electronics calibration

The ADC channel number of the electronics was calibrated by measuring the response of each channel to an input pulse supplied by a pulse generator. The pulse was distributed to all the electronics channels by pulsing the ground plane for a range of input voltages. This distributed the pulse evenly across the entire pad plane. The input voltage is plotted as a function of the measured ADC channel in Fig. 1.3 for every channel. The small variation in each channel can be seen as the wide band around each measurement point. A linear fit is performed to get the best fit line which provides a reference line which each channel is calibrated to. The right panel shows the resulting distribution of channels after calibration. This is a relative calibration technique with the intent to calibrate the varying gains in each channel relative to one another.

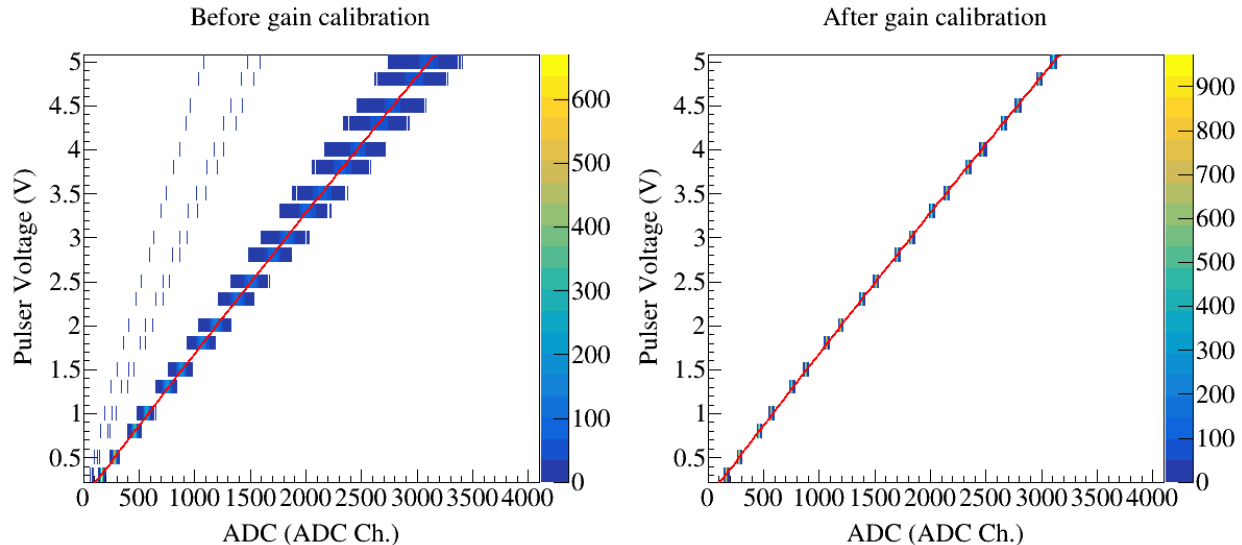


Figure 1.3: Calibration of electronics

1.2.4 Anode gain calibration

As mentioned earlier, the anode wires were separated into 14 independently biased sections. The high voltage of sections 12 and 14 were reduced during the experiment due to high currents being observed on the wires. The wire section voltages were lowered once and adjusted once again. Out of all the runs used in the analysis in this thesis .1, the anode sections 12 and 14 were lowered to 1085 V for runs 2272-2371 and set to 1214 V for all the other runs. By lowering the voltage on these anode wires, the gas gain is lowered as compared with all the other anode wire plane sections which operate at 1460 V. To account for the drop in gain, in the software we increase the gain of the pads which lie above these anode wires to match the gain in the other channels. To do so, we compare the energy loss in the high gain sections to the low gain sections to get the relative calibration factor.

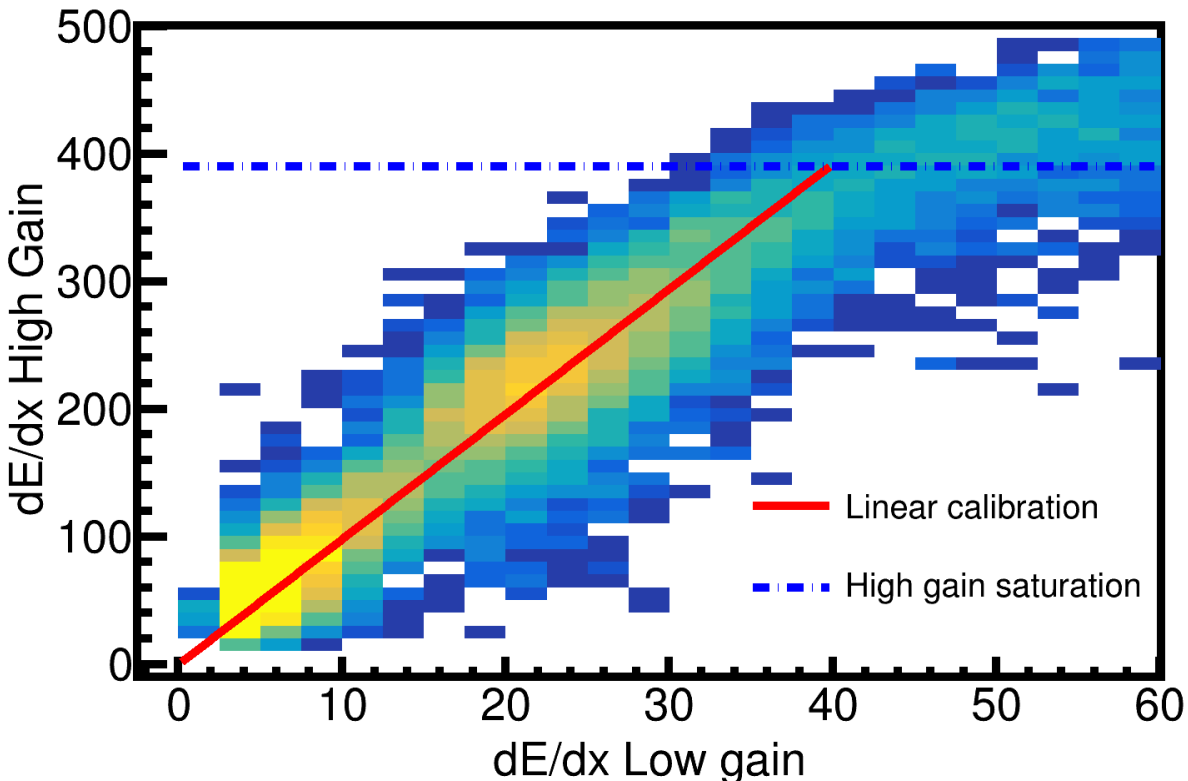


Figure 1.4: Calibration of low high.

Figure 1.4 shows the correlation plot of $\langle dE/dx \rangle$ of the high versus the low gain sections. The

effects of the high gain channel saturation can around a value of 400 ADCmm^{-1} and plateaus, whereas the low gain does not. A linear fit was performed for the calibration between the high gain channel $h_c = G \cdot l_c$, where l_c is the value of the low gain channel and G is the gain factor. In the case where the low anode voltage was 1214 V, the gain factor was 9.8 whereas in the case of 1085 V, the gain factor was ????. The calibration factor was applied inside of the decoder task. A map of the channels which are impacted by the low anode wire voltages and the relevant gain was input into the software. In the decoder task the raw ADC spectra was multiplied by the input gain for a given channel. The thresholds of those channels also were multiplied by the same factor since the noise levels were also artificially magnified by the same gain factor.

1.2.5 Extending the dynamic range of the Electronics

Using a TPC for measurements of HIC in nuclear physics presents a different set of challenges as opposed to higher energy experiments. Typically in higher energy experiments the charge of particles is Ze , where $Z=1$. Also, the particles are traveling at higher energies in which the energy losses are near or close to the minimum in the energy loss curve. The dynamic range of electronics in such experiments can cover a wide range of particle energies in the energy loss curve. In nuclear HICs, we are interested in measured particles ranging from $Z=1-3$ resulting from the collision, and even higher in some applications. As seen in Eq. ??, the energy loss is proportional to Z^2 ; the energy values in nuclear HIC of intermediate beam energies (around 300 MeVA) in which the resulting particles are at much lower energies which are in the $1/\beta^2$ region. The energy range and particle types covered by the electronics are significantly limited by the dynamic range limitations of the electronics as the charge of a particle increases and the velocity decreases.

Several TPCs have tried to address this issue by having regions of low and high gain, either in amplification gain or in electronics gain. Here we run into the issue that high velocity particles will have little to no signal in the low gain regions. At lower velocities, particles will deposit much charge over the low gain regions but will saturate the high gain regions, whose charge values are usually

lost. Only within the dynamic range will tracks have the best momentum resolution, outside the dynamic range clusters will be missing in the sections which depend on the track velocity, lowering the momentum resolution of tracking. There are ongoing efforts in the nuclear community to develop new electronics which hope to mitigate these persistent issues in TPC electronics CITE HERE, by being able to switch to a lower gain value when the maximum range is reached. Though, it is quite useful to develop a software technique which may extend the dynamic range of TPC electronics without the use of external hardware, especially in experiments which have already been performed with preexisting electronics technologies.

In TPCs, the effective dynamic range can be very different from the single channel dynamic range depending on the application. Typically TPCs are operated inside of a magnetic field for reconstructing momentum of each particle, which requires sub-millimeter precision in the position determination of the track path. This is achieved by averaging the charge distribution over several pads. Therefore the effective dynamic range is related to the relative charge values of adjacent pads (between the center pad and outside pads). For example, to measure minimum ionizing particles the signal to noise ratio of the pad with the smallest charge in the distribution should be some reasonable value above noise, say at least 6:1 signal-to-noise ratio (SNR). From Section ??, we know the central pad in the cluster holds 80% of the total charge, where as the two adjacent pads each hold the remaining 10%. If we require the adjacent pads to have a SNR of 6:1, then the central pad would have a SNR of 50:1. Considering this is the SNR for minimum ionizing particles, and the maximum SNR in a channel is 800:1, this means the effective dynamic range in the TPC is roughly 16 times that of minimum ionizing particles, if we intend to have adequate position and tracking resolution.

The dashed lines and vertical blue bar in Fig. 1.5 are separated by a factor of 20, representing the typical effective dynamic range in a TPC. This dynamic range estimate should be regarded as approximate because the energy loss fluctuates significantly about the most probable energy loss, with a long “Landau” like tail, as described by Bichsel [4]. Nevertheless, the blue dashed lines and vertical blue bar illustrate that the range of energy losses sampled in a fixed gain readout system

is limited. One can change the gain and shift the energy loss range that can be sampled, but the dynamic range itself cannot be increased.

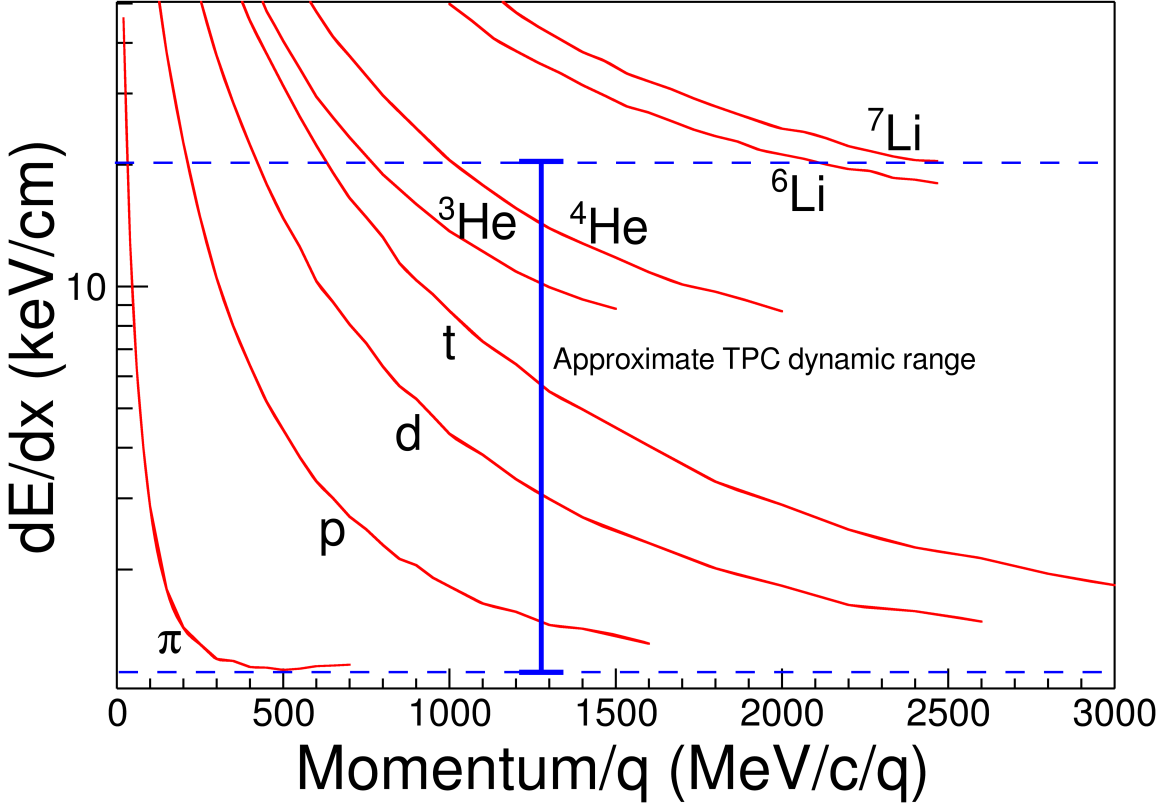


Figure 1.5: The expected dE/dx lines of different particles are given in red as calculated by Geant4. The approximate dynamic range of the TPC is shown by the vertical bar for the gain setting used in the experiment. Anything outside of this region would be saturated to some degree.

The rapid increase in the stopping powers at low momentum illustrates the degree to which the effective dynamic range can be exceeded and highlights the problems encountered in studies of intermediate HICs, in which light particles with low momenta are abundantly produced along with highly charged particles. Similar problems are encountered when TPCs are used as active targets in direct reaction studies with rare isotope beams [?]. Several techniques have been employed to increase the observable range of energy losses; typically by lowering the electronics gain of selected readout channels, or by changing the gas amplification at the readout plane in certain areas of the TPC ?????. The results of changing the gas-gain, or the electronics gain, are rather similar in that reducing the gain to sample a range of higher energy loss makes the TPC effectively blind to

minimum ionizing particles in the regions of lower gain.

1.2.6 Experimental Pad Response Function

The pad response function of the TPC was extracted from non-saturating hits and clusters in tracks at various track crossing angles. As in Fig. 1.1, we postulate that the PRF is a function of the total charge deposited in a cluster $Q = \sum_i q_i$, and the difference in position of the center of the i^{th} pad, x_i , to the mean position $\bar{x} = \sum_i x_i q_i / Q$, defined as $\lambda_i = x_i - \bar{x}$. The PRF is simply defined as the charge fraction of each pad as a function of λ , as shown in Equation 1.1.

$$PRF(\lambda_i) = \frac{q_i(\lambda_i)}{Q} \quad (1.1)$$

Averaging over many events in the experimental data, the resulting PRF for the S π RIT TPC is shown in Fig. ???. Here we see the deviations from the expected analytic Gatti distribution (black curve), whereas fitting with a two parameter Gaussian function (red curve) gives a better description of the data, Eq. 1.2, with the two parameters being the normalization coefficient, N_0 , width σ , and with a mean value assumed to be 0.

$$PRF_{\text{Gaus}}(\lambda) = N_0 e^{\frac{-\lambda^2}{2\sigma^2}} \quad (1.2)$$

The shape of the PRF depends on the crossing angle of the track [5], which determines how wide the charge is distributed along the wire. Figure 1.6 shows the PRF of π^- tracks versus the crossing angle θ of the track. The PRF gets wider starting from 90° and until where we switch clustering directions at 45° ; if we did not switch clustering directions the PRF would become wider until it was a uniform distribution and there was no position resolution. Switching from x to the z direction clustering the opposite trend is seen where the PRF becomes narrower going from 45° to 0° , as the position resolution gets better.

A Gaussian fit was performed were performed to the experimental data with 5° width bins from $0^\circ < \theta \leq 90^\circ$. Figure 1.7 shows the two parameters resulting from fitting the the Gaussian function

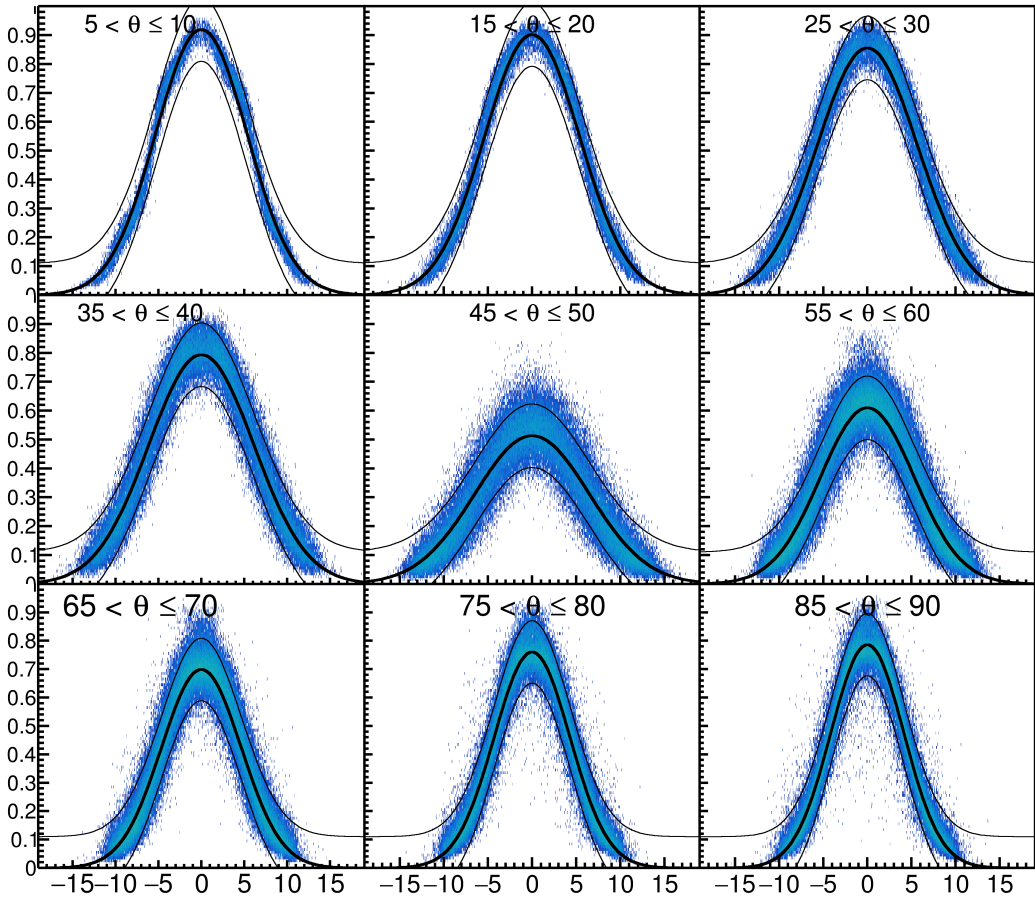


Figure 1.6: PRF response from π^- data.

given in Eq. ?? are plotted versus θ . A 4th order polynomial fit of these parameters allowed for interpolating for any given θ value as seen by the black line.

1.2.7 Method of Desaturation

We will use the term “desaturation” to describe the process of correcting the charge values of the saturated pads. Figure 1.8 shows a typical situation of saturated signals in a given cluster of hits. When an avalanche causes a large enough induced signal, it is the pads directly underneath which collect the largest charge becoming saturated; denoted here as $q_{2'}$ and $q_{3'}$. Pads further away collect less charge and typically are not saturated; the non-saturated pads are denoted here as q_1 and q_4 .

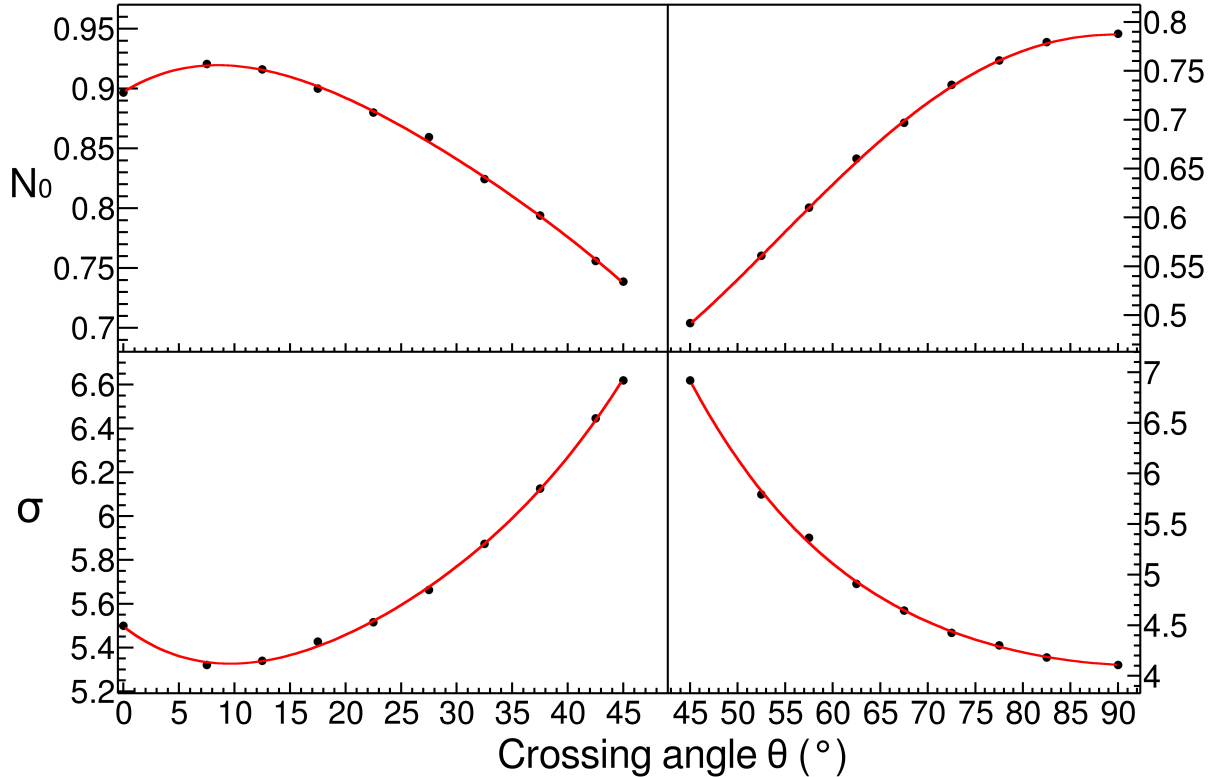


Figure 1.7: Parameters N_0 and σ as a function of the crossing angle θ with the 4^{th} order polynomial fits.

Though the true charge value in the saturated channels are lost, we know that the distribution of all charges must follow the PRF which is a fixed feature of all TPCs, and has been experimentally measured above. From the tracking information, we know a given clusters crossing angle and can interpolate to get the corresponding parameters for the PRF described in Fig. 1.7.

We assume the distance of each pad to the track, λ_i , is fixed, defining the fraction of charge each pad receives as given by the $PRF(\lambda_i)$ function. To determine the best estimate for the charge values of each saturated pad, a chi squared function is minimized,

$$\chi^2 = \sum_i \frac{(q_i^{\text{obs}} - q_i^{\text{expect}})^2}{q_i^{\text{expect}}}, \quad (1.3)$$

where q_i^{obs} are the non-saturated charges and q_i^{expect} are the charge values expected from the

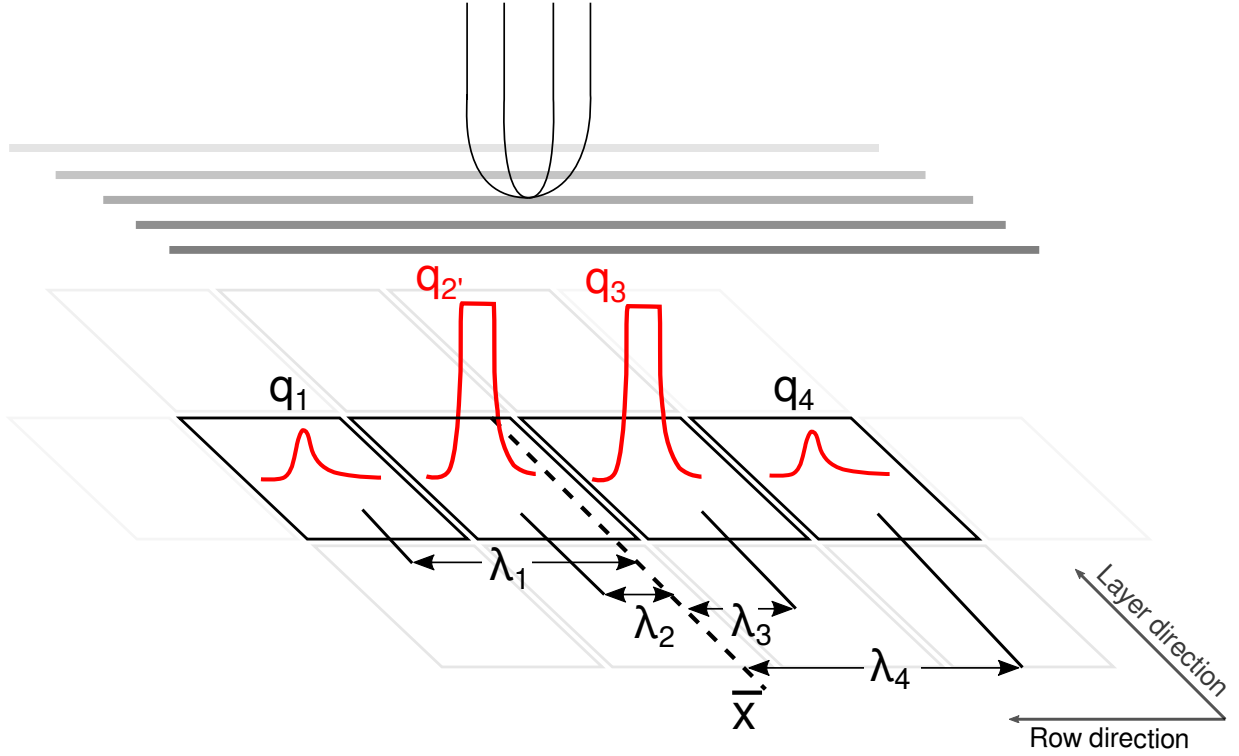


Figure 1.8: A typical case of a saturating event. The red pulses represent the time bucket signal for each collected charge. The pads directly underneath the avalanche point, q_2' and q_3' , are saturated while pads farther away, q_1 and q_4 , are not saturated.

PRF calculated as $q_i^{\text{expected}} = Q \cdot PRF(\lambda_i)$. The saturated charge values q_i' are treated as unknown variables and are allowed to vary in the χ^2 minimization; the values calculated by the minimizer are added to the total expected charge Q .

Tracks which saturate pads in the high anode wire voltage region are not saturated in the low anode voltage region. By comparing the $\langle dE/dx \rangle$ values of these two sections, we can directly measure the success of the desaturation in the high gain regions. While this desaturation technique avoids the need to lower the gain of any region, the low anode voltage region proved to be a direct measurement of the success of this technique.

Figure ?? shows the the $\langle dE/dx \rangle$ values of the high gain region compared with the calibrated low gain region. The effect of saturation can be seen in the high gain region for the uncorrected data above values of 400 ADC/mm where the values plateau, where as the low gain region still

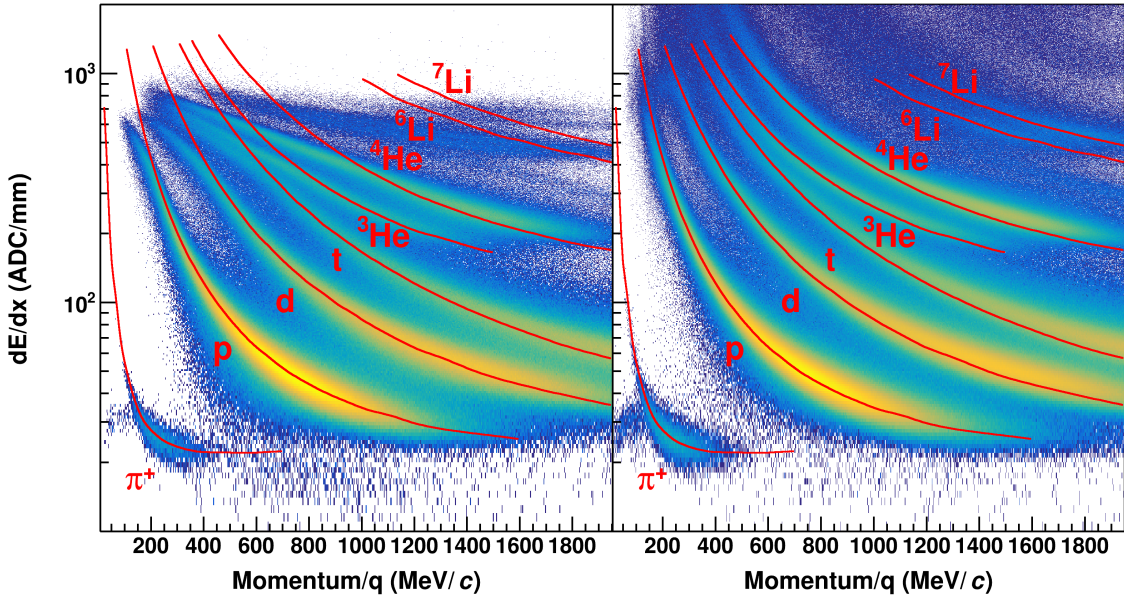


Figure 1.9: Uncorrected (left panel) and desaturated (right panel) collision data at polar angles of $\theta < 40^\circ$ and azimuthal angles between $-80^\circ < \phi < 80^\circ$

returns accurate values¹ Below this value the electronics are not saturated, and therefore the high and low gain sections agree.

After applying the desaturation method, the correlation between the high and low gain sections is restored, as seen in Fig. ???. From this comparison, we can approximate that the correction has corrected the high gain sections to agree with low gain sections to values of 2000 ADC/mm, increasing the dynamic range by a factor of at least 5.

The success of the desaturation becomes more clear when looking at the particle identification (PID) lines. In the following PID plots the red lines represent the most probable energy loss as given by Geant4 straggling functions. A linear calibration was performed to convert keV in Geant4 to ADC in the experiment given by $ADC/mm = 19; keV/cm$.

There are pronounced PID lines of several particle species in both the uncorrected and corrected cocktail beam PID shown in the subplots of Fig. ???. The uncorrected data in the left panel shows the effects of saturation; the PID lines deviate from their theoretical expectations starting at around 400 ADC/mm eventually reaching a plateau. After applying the desaturation technique – in the

¹Un-calibrated ADC channels in arbitrary units.

right panel – we see a large improvement, most notably for the He and Li particles, which suffer the most from saturation and even 6Li and 7Li can be separated. A more subtle improvement of the lighter particles, (p, d, t), can also be seen in the PID lines at lower momenta.

A similar effect is seen in the experimental collision data. In Figure 1.9 though the PID suffers from more background and inefficiencies than the cocktail beam we see a similar improvement in the PID lines when comparing before – the left panel – and after applying desaturation – the right panel. Notably the largest improvement is the separation of particle species at lower momenta and the separation of the Li species into 6Li and 7Li . In these regions, there was little to no PID resolution before desaturation.

The dynamic range was extended by at least a factor of 5, as demonstrated by the improved PID lines, and quantified by direct comparison to low gain sections of the TPC.

1.2.8 Space Charge Corrections

As the beam passes through the field cage it ionizes the gas creating electron-ion pairs. The drift velocities of the ions are typically 10^4 times slower than the electron drift velocities [?, blumrol] Any source of ions have the potential to build up creating a positive space charge distorting the drifting electrons, biasing the track momentum. There are several regions of the TPC in which ion are created. The largest source of positive ions is created in the avalanche process near the anode wires. These ions slowly drift toward the cathode. If the gating grid is closed the ions will terminate there; though it opens occasionally for 11 μs the ions only move 1 μm in this time and will be captured by grid when it closes. For this reason, the source of ions resulting from the avalanche region is negligible.

The other source of ions come from the primary ionization produced by the beam and reaction products in the detector gas. The energy loss $\langle dE/dx \rangle \propto Z^2$, where Z is the charge of the particle type. Because the charge of the un-reacted beam is around $Z \approx 50$, the ionization due to the beam is a factor of 2.5×10^3 times that of the light charged particles which mostly are of charge $Z = 1$. It is the largest source of positive ions in the TPC.

NEED TO PUT IN ABOUT THE GATING GRID LEAK

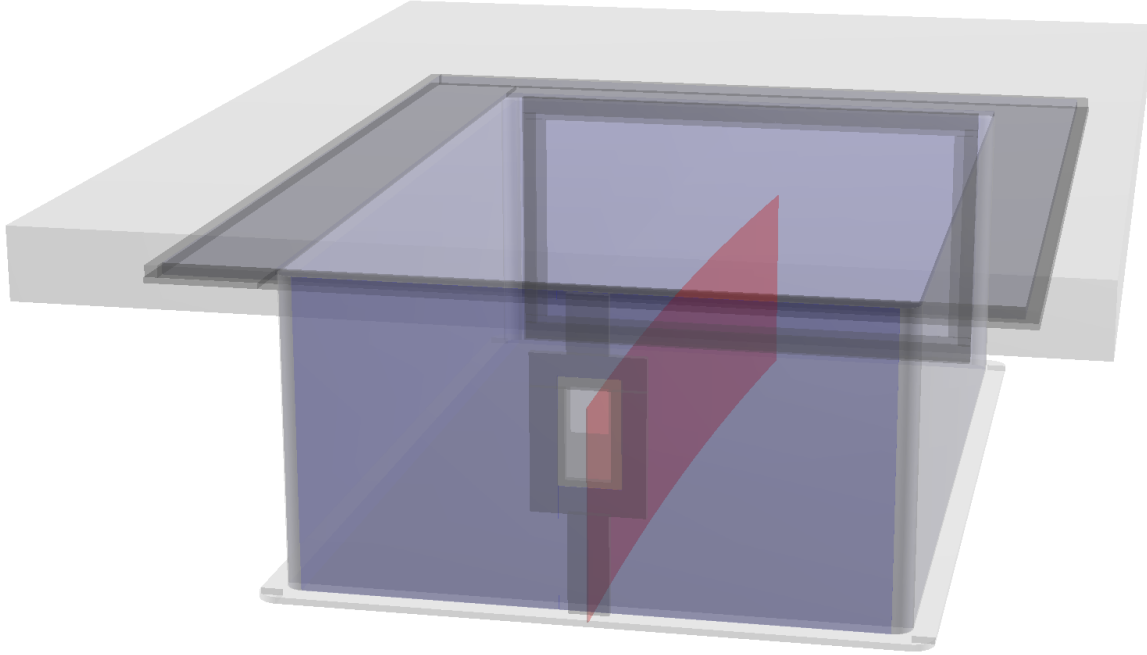


Figure 1.10: Location of space charge in ^{132}Sn

The beam is positioned about 25cm below the anode plane in the TPC. It takes electrons approximately $5\mu\text{ sec}$ to drift to the anode plane whereas it takes the ions $5 \times 10^4\mu\text{ sec}$. The beam rate in the experiment varied around a value of about 10kHz, which has an average occurrence of 1 beam every $100\mu\text{ sec}$; this is shorter than the time it takes for the ions to terminate on the cathode plane, resulting in a build up of positive ions. Figure 1.10 gives an idea of the shape of the sheet of space charge carved out by the beam path. The ions from each beam create a line charge which drifts towards the cathode with a constant velocity. The average distance between sequential ion paths is about $25\mu\text{m}$ apart, therefore we expect the average number of beam paths that compose the sheet charge is around 1440 tracks – where the distance to the cathode is 29.6 cm. Though the arrival time of each beam track is random, the large number of tracks and small inter beam spacing allows us to approximate the sheet charge as an uniform sheet charge.

The secondary beams entering the TPC are also composed of many species of particles dis-

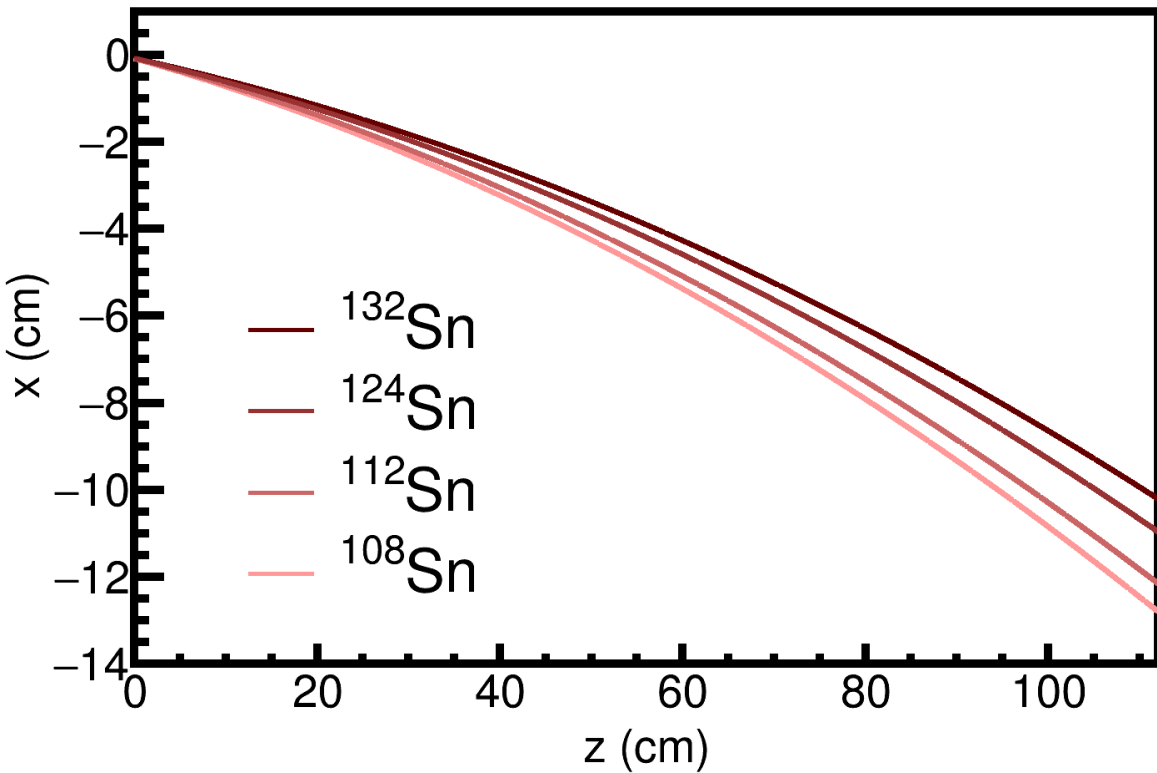


Figure 1.11: Beam path of the experiments

tributed in a finite range around the target beam. Assuming a beam of ^{132}Sn were the energy loss in gas is 11.2 keV cm^{-1} , using the number of beams above, the conversion to electrons given in ??, and the beam path length of 135 cm, the total charge density expected is $3 \times 10^{-8} \text{ C m}^{-2}$.

The electric potential can be calculated by solving Poisson's equation,

$$\nabla^2 \phi = \rho, \quad (1.4)$$

where ϕ is the electric potential and ρ is the free charge. Since the Dirichlet boundary conditions of the field cage are defined by the cathode, walls, and pad plane, a numerical solution to the electric potential is solved through the ??? technique. The electric field is simply the gradient of the potential $\vec{E} = -\nabla \phi$.

To reduce the need to compute a new electric field for a new value of the space charge, we notice that $\vec{E} \propto \rho$, we can therefore solve the electric field for a certain reference charge value ρ_o , and scale

the solution for any other free charge ρ by the ratio ρ/ρ_o . The full magnetic field map is provided by the SAMURAI collaboration [6]. The velocity field map can be calculated from Eq. ???. The path an electron drifts through this velocity map is propagated by using a time stepped 4th-Order Runge-Kutta integration from a given starting point of the electron. We do not add details of the electric field around the anode wires which is only relevant for the small gap between the ground and anode plane. Over this small gap the space charge corrections have very little effect.

The correction map is calculated by starting from the anode y-position and the measured position on the pad-plane (x,z), and stepping backward in time in the Runge-Kutta integration through the velocity field map until the electron reaches the measured y-position, which is split into a grid that fills the 3-dimensional volume of the field cage.

The correction is handled within the STCorrection task in the software. A data base of the sheet charge values for every run is read in and the electric field is calculated for the reference charge for a given beam path. The electric field and velocity map is scaled by the ratio of the space charge in the particular run and the reference run ρ/ρ_o and the correction map is calculated. The measured clusters value (x,y,z) position is input into the correction map which interpolates and outputs the correction values dx and dz which correspond to that cluster. The cluster position is shifted to new positions $x' = x + dx$ and $z' = z + dz$, before going on to the momentum and vertex finding algorithms.

It has been shown before that the amount of space charge present in the chamber is related to observables such as the distance of closest approach of each track to the vertex point [7]. In the presence of no space charge, you would correctly expect the distance of closest approach of each track to the vertex point would be a distribution centered around the true vertex location. Since the tracks are distorted by the space charge, which affects different regions of the TPC differently, a bias is introduced to the measured vertex location and widens the distribution to vertex of each track.

An example of the distortion map in the TPC is shown in Fig. 1.12 with left-going tracks shown in blue, and right-going tracks shown in green; the vectors show the direction of distortion and

their magnitude have been magnified by ??? times to show the detail. The dashed lines show the effects the track shifted due to the space charge map where left and right-going tracks are affected differently. Right-going tracks tend to higher momentum values and the left-going tracks going to lower momentum values, for positively charged particles.

The inset figure of Fig. 1.12 shows the shift in the x-position distance to vertex for the displaced left-going track given by ΔV_x , with the opposite direction for right-going tracks. We will define the DOCA for left going tracks as V_x^L and for right-going tracks as V_x^R . We are able to measure the amount of distortion the space charge creates by measuring the difference between the most probable values of the left-going and right-going tracks which we define as $\Delta V_{LR} = \Delta V_x^L - \Delta V_x^R$ as seen in Figure 1.13.

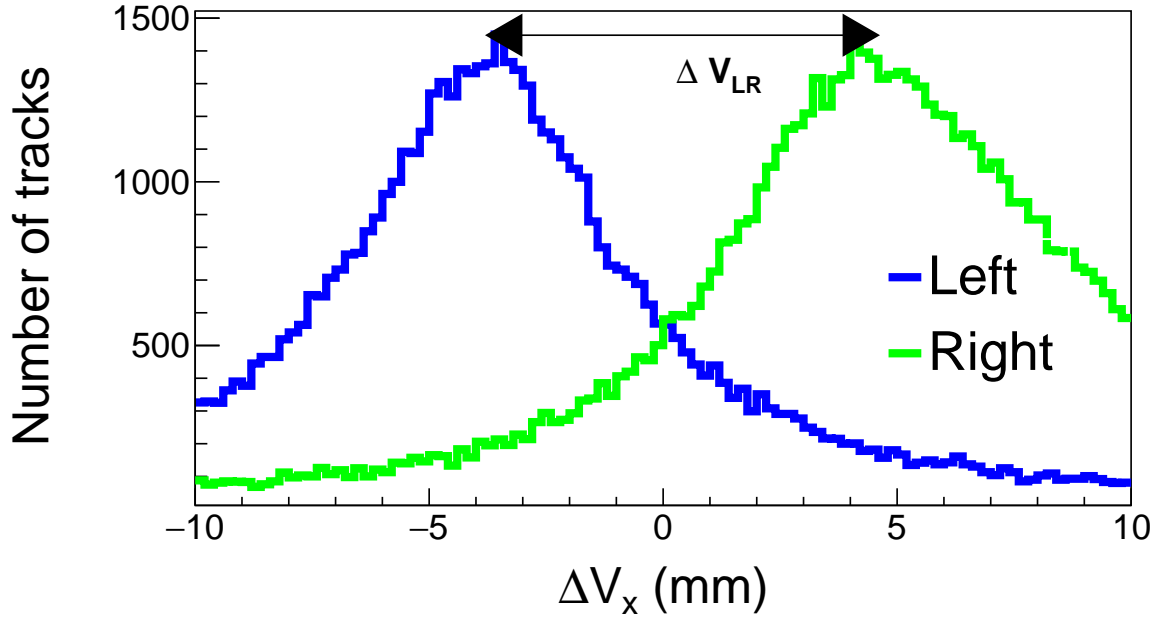


Figure 1.13: ΔV_x distribution for left-going and right-going tracks in the TPC for the

The average beam rate was recorded in each experimental run and slightly varied from run to run, due to beam production variations. The amount of space charge present in the field cage is directly proportional to the beam rate; therefore ΔV_{LR} is also proportional to the beam rate as

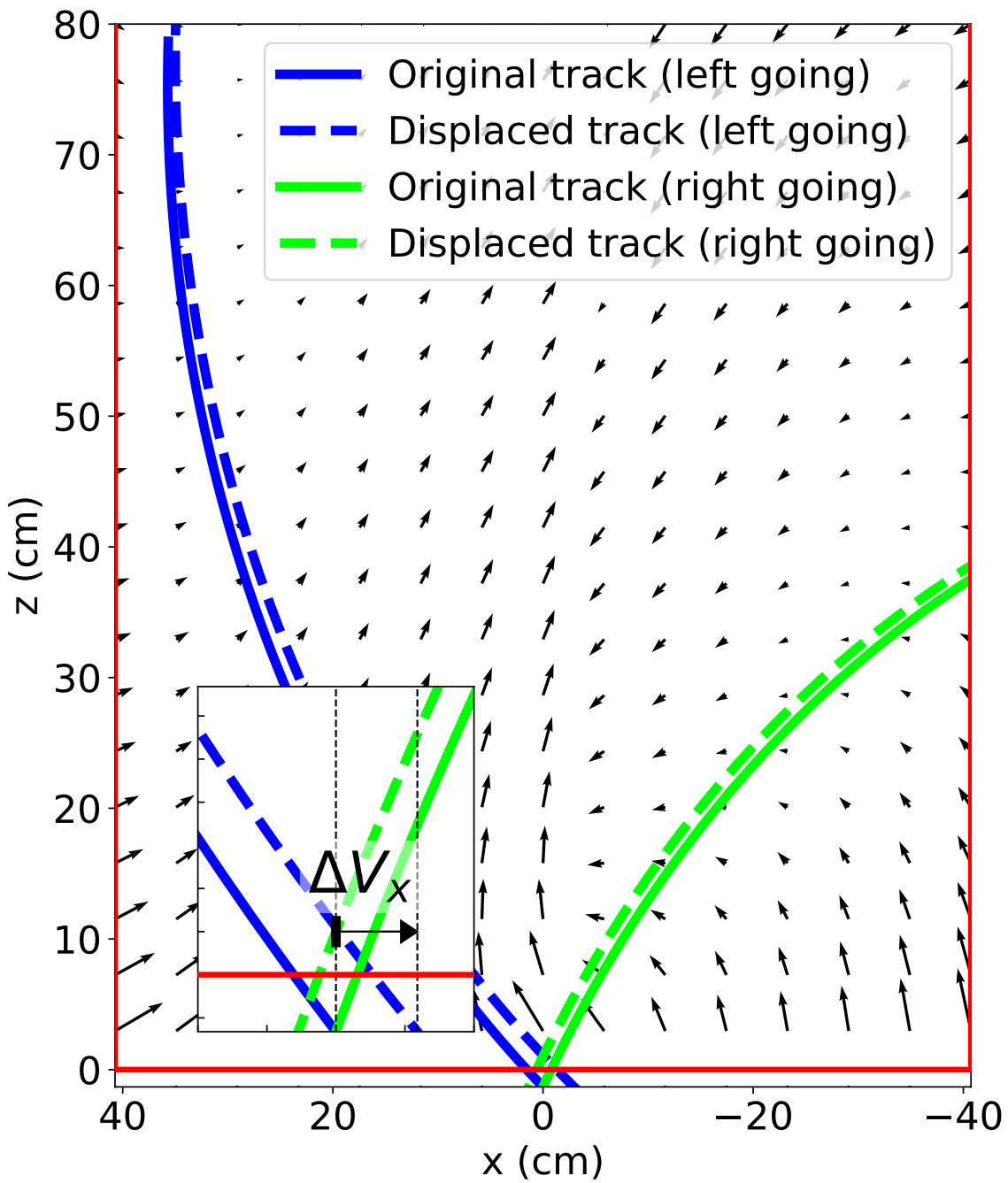


Figure 1.12: Shift of tracks

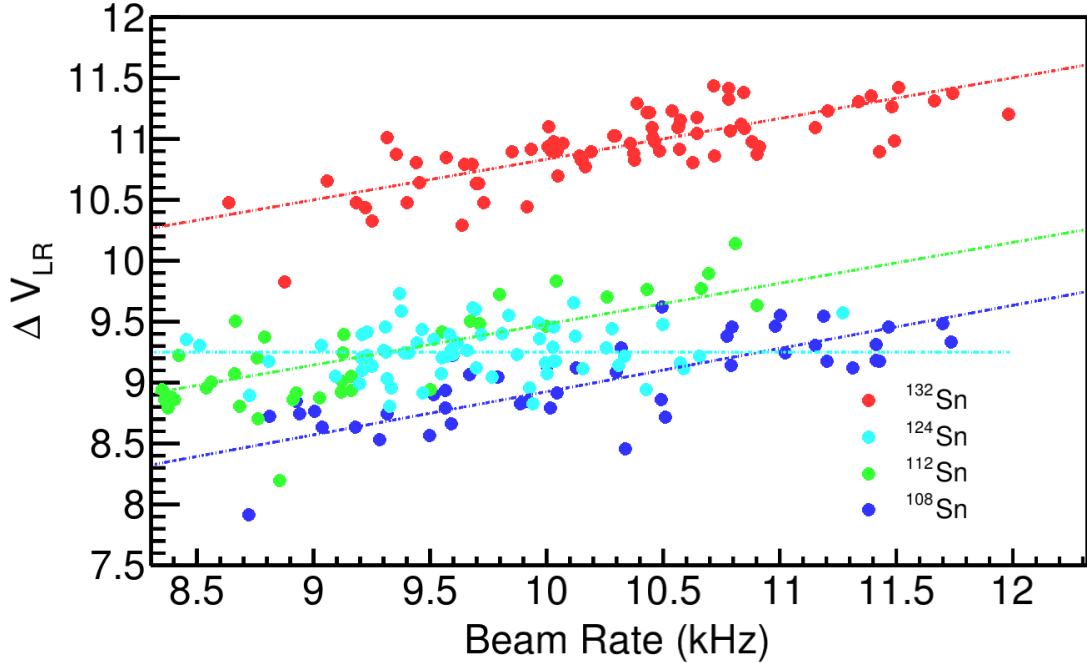


Figure 1.14: ΔV_{LR} versus the beam rate for all systems with the fitted function.

shown in Fig. ???. The only parameter in the space charge correction algorithm is the surface charge density σ_{SC} . Varying σ_{SC} for a wide range of values the ΔV_{LR} observable is measured and plotted in the left panel of Fig. 1.16. The surface charge density which gives $\Delta V_{LR} = 0$ is taken to be the estimate for the average amount of space charge present.

This is done for several runs which vary in beam intensity though the solution for the estimated space charge value will be different. Since the surface charge density is proportional to the beam rate, a linear fit gives good agreement for interpolating the surface charge values as a function of beam rate. Figure 1.16 shows the relation of the dependence of the space charge as a function of beam rate for the ^{132}Sn system.

Following this algorithm the space charge is estimate for each run and system. Figure 1.17 shows the summary of the extracted space charge values for each secondary beam. The linear fits relating the space charge density to the beam rate for each system is shown in Fig. 1.15 where the space charge value is inferred from the measured beam rate. Notice that in the $^{112}\text{Sn} + ^{124}\text{Sn}$

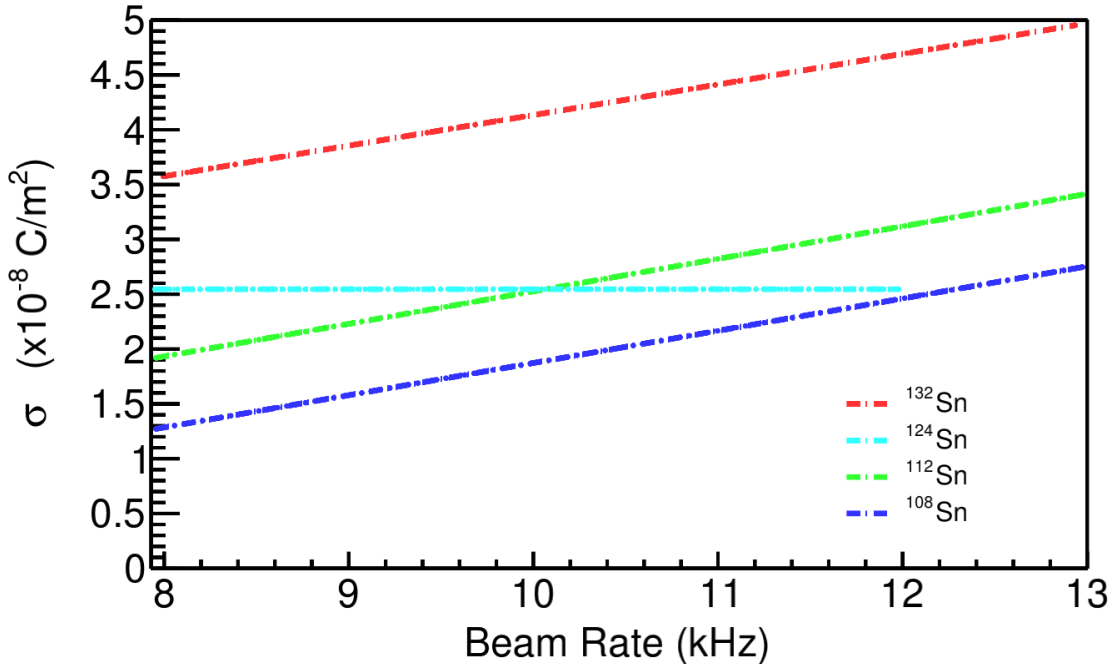


Figure 1.15: Space charge fit function versus the beam rate for all systems. These are the assumed functions we use for interpolating the space charge value from the beam rate.

system a constant value of was assumed since the beam rate did not span a large enough range to warrant a more detailed analysis.

Adding the BDC vertex greatly improves the momentum resolution of the track fitting, but there is a systematic shift when as compared with the momentum value without using a vertex as an extra constraint. Since the space charge affects right-going and left-going tracks differently making right-going tracks differently than left-going tracks, it appears they no longer originate from the BDC which is not affected by the space charge. For tracks at polar angles of $\theta < 40$ deg, the disagreement between momentum values with and without the BDC are much less because the projection of the track does not disagree as much with the BDC point as shown in Fig. 1.19a. Figure 1.19b shows the momentum value of tracks going at polar angles of $\theta > 40$ deg are more sensitive to small changes in the BDC when including it as an extra constraining point. After correcting for the space charge, adding the BDC point as an extra constraint on the track does not bias the reconstructed momentum value for either $\theta < 40$ deg or $\theta > 40$ deg, which has the greatest improvement, as seen in Fig. 1.19c

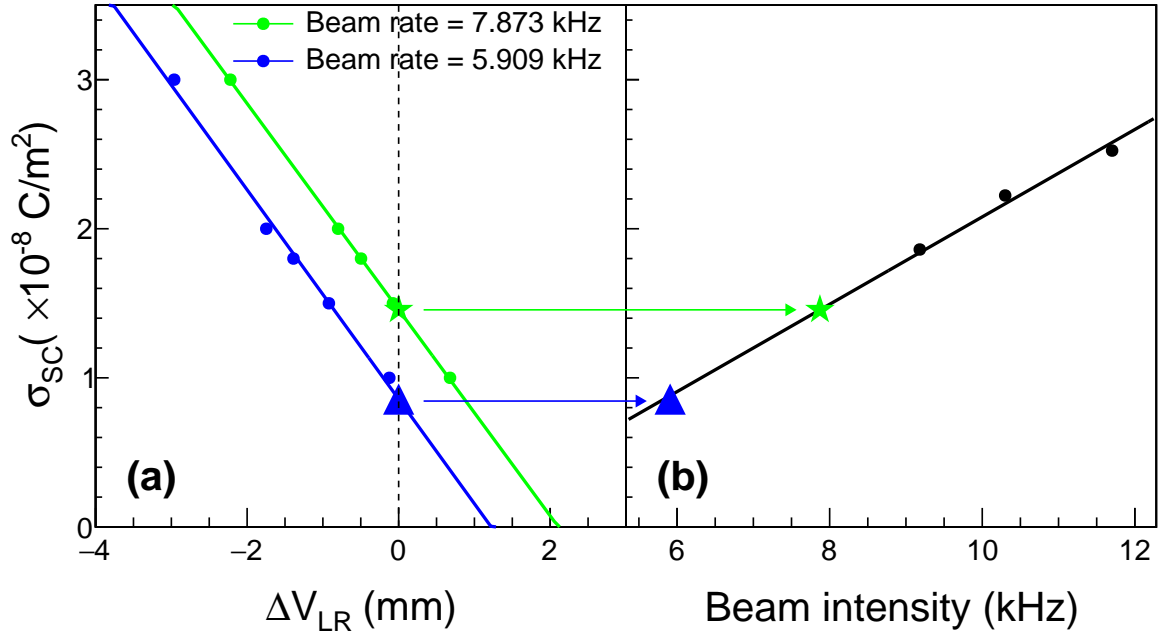


Figure 1.16: Space charge relation

and Fig. 1.19d respectively. Recall that only the relative distance between left and right-going tracks was minimized; there was no guarantee that the corrected tracks coincide with the absolute BDC position at the target. This is one of the evidences of the correction's success. The others being the agreement with the expected cocktail calibration beam as described above. Later we will show how the space charge corrects the momentum distributions of left and right-going pions in the TPC.

1.3 Monte Carlo Simulation

The monte carlo (MC) simulation is composed of two separate simulations. The first simulation is an accurate model of the fundamental interactions of a particle passing through the various materials in the TPC; to accomplish this we have modled everything in Geant4 which also provies a particle generator. A scale model of field cage, front window, front window frame, pad plane,

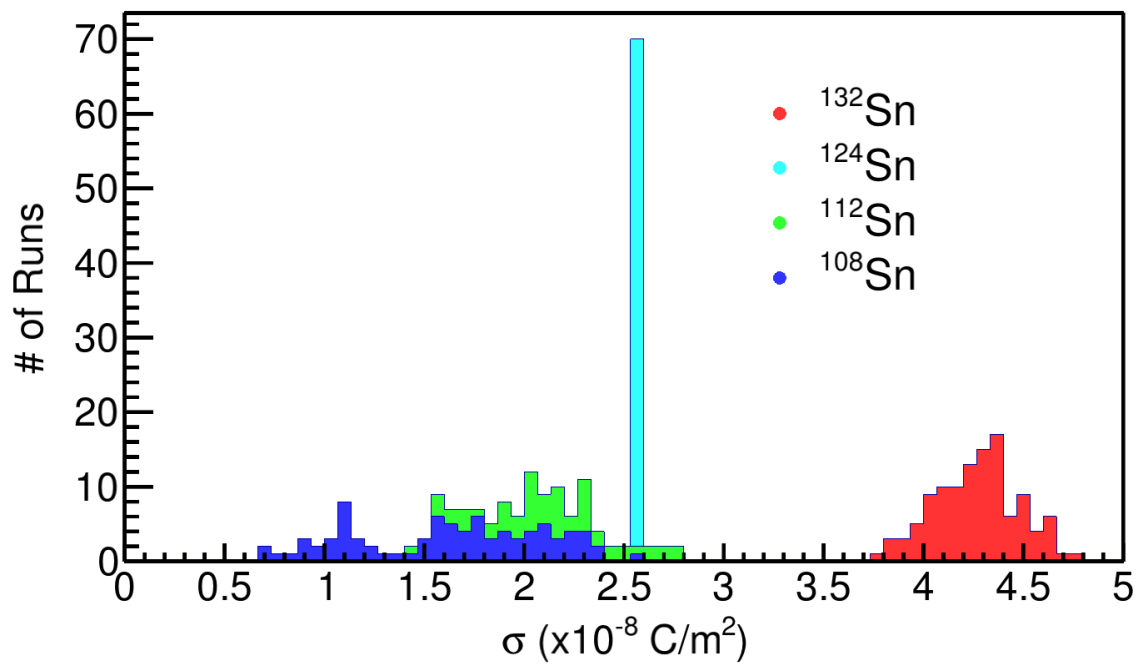


Figure 1.17: Distribution of estimated space charge densities for each beam type.

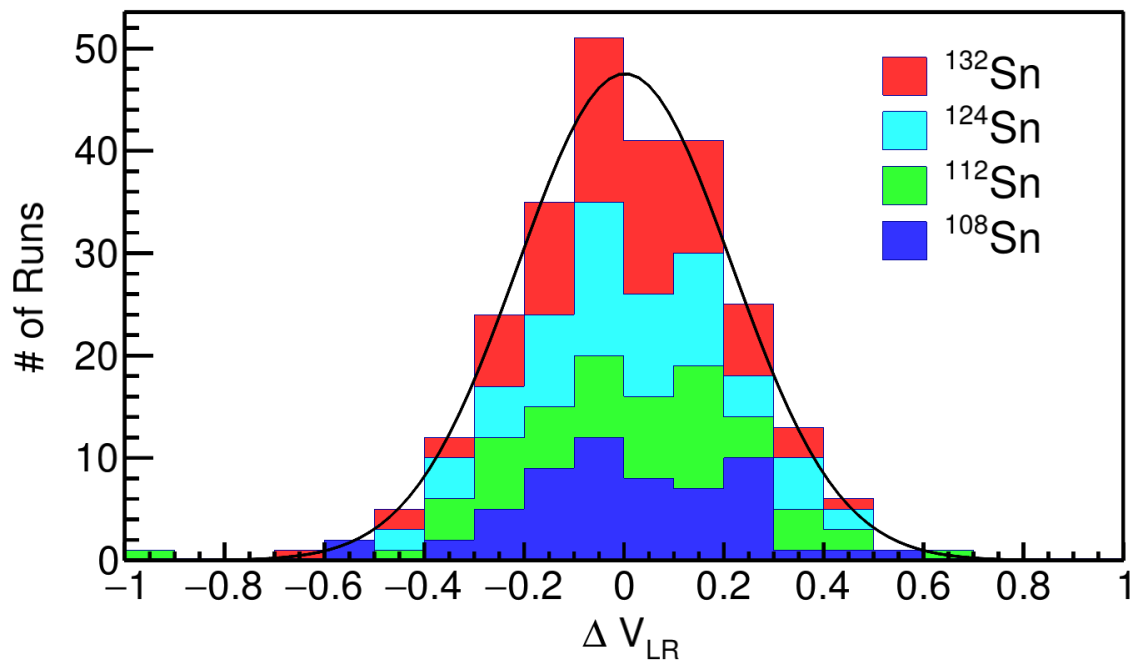
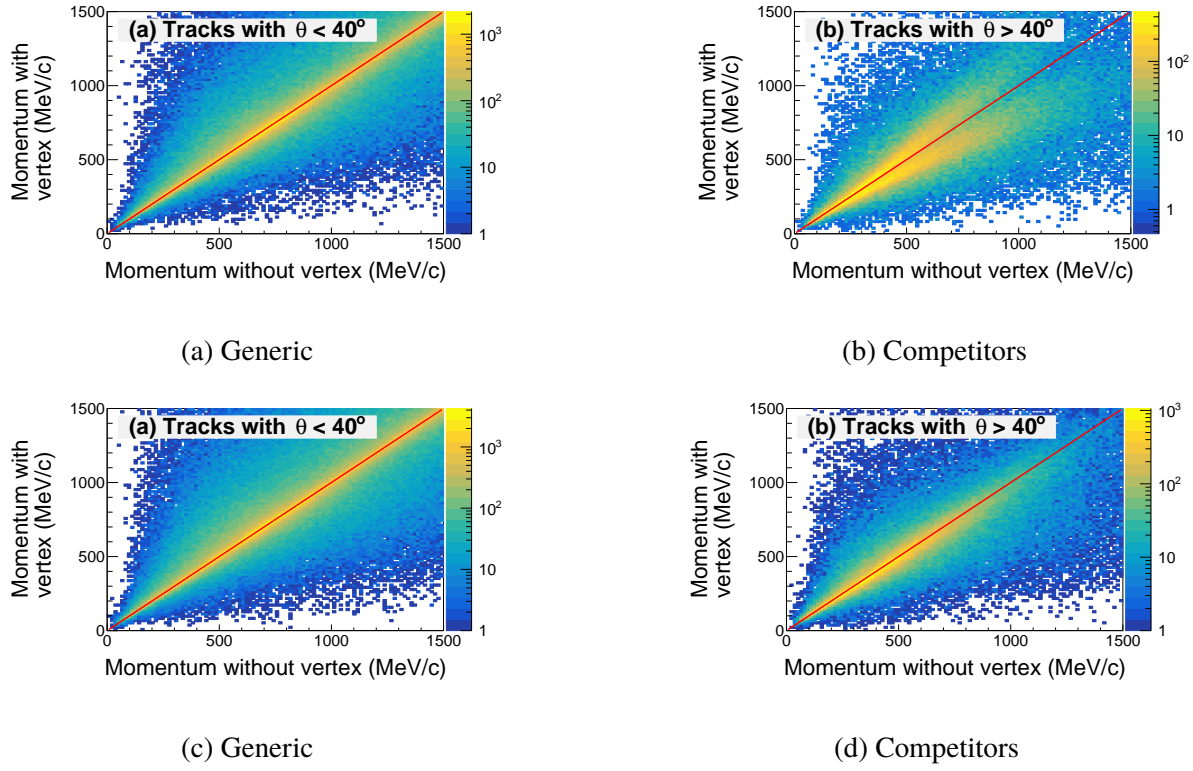


Figure 1.18: Residuals in the fitted line of ΔV_{LR} observable for all systems.



and aluminum top plate are modeled with the correct material type and dimensions assuming P-10 gas at a density of 1 atm. The magnetic field map of the SAMURAI dipole magnet was imported into Geant4 as well after assuming rotational symmetry along the axis perpendicular to the pole face. Along with the energy loss and particle transport, Geant4 also handles multiple scattering, and particle decay. The output of the particle generator is a series of energy loss points which contain the amount of energy lost in keV cm^{-1} and the location of the energy loss in Cartesian space (x, y, z).

In the second part of the MC simulation the physical processes involved in the operation and measurement of the TPC are simulated, such as the electron drift, avalanche process, and all processes involved in the signal creation in the electronics; to simulate the detector response of the MC event. This is separated into several software tasks; the drift, pad response, and electronics tasks. In the following section we will discuss in detail the tasks involved in simulating the TPC response. The discussion of Geant4 is not covered here and is left to the reader to explore.

Electron Transport Gas Properties	
Drift velocity	5.53 cm μs^{-1}
Transverse diffusion	240 $\mu\text{m cm}^{-1/2}$
Longitudinal diffusion	340 $\mu\text{m cm}^{-1/2}$
Gas Ionization	26.2 eV

Table 1.5: An overview of the properties of the TPC

1.3.1 Drift Task

The first step of the drift task is to convert the primary ionization points of the MC track, provided by Geant4, into the total number of electrons, N_{e^-} . The average number of electrons created in a gas can be described as,

$$N_{e^-} = \frac{\Delta E}{I}, \quad (1.5)$$

where the ionization coefficient of P10 gas, I , (Table 1.5) and ΔE is the energy loss deposited in units of eV. Since the electric field set up by the field cage is uniform for the most of the area covered by the pad plane, we assume a straight line trajectory for each electron until it reaches an anode wire. The total length drifted from the initial primary ionization point to the final anode wire is given by L_{anode} .

Drifting electrons exhibit stochastic motion which can be described by a diffusion process occurring along the direction of travel (longitudinal) and transverse to the motion. The longitudinal, c_l , and transverse, c_t , diffusion coefficients are determined by Garfield++ calculations in the presence of a 0.5 T magnetic field, given in Tb. 1.5. The diffusion process is modeled by randomly sampling the from a Gaussian distributions describing both directions and adding the shifts to the electron final position. The stochastic deviation in the transverse direction, dr , is randomly sampled from,

$$dr = e^{-\frac{r^2}{2\sigma_t^2}}, \quad (1.6)$$

where $\sigma_t = c_t \cdot \sqrt{L_{anode}}$. The Cartesian directions are given by $dx = dr \cdot \cos(\alpha)$ and $dz = dr \cdot \sin(\alpha)$, where α is a random angle from 0 to 2π , since there is no preferential angle of emission in the transverse plane. The shift associated with the longitudinal diffusion, dl , is randomly sampled from,

$$dl = e^{-\frac{t^2}{2\sigma_l^2}}, \quad (1.7)$$

where $\sigma_l = c_l \cdot \sqrt{L_{anode}}$.

The total drift time, t , is calculated as,

$$t = \frac{L_{anode} + dl}{v_d} + t_{offset}, \quad (1.8)$$

where v_d is the drift velocity. The parameter t_{offset} aligns the MC time bucket spectrum with the data; the data time bucket zero does not correspond to the same y-position in the MC for the same time bucket position. The electron is assumed to terminate on the nearest anode wire which fixes the z-position that of the anode wire.

The total number of electrons produced in the avalanche process of a single electron was simulated in Garfield++ as seen in Fig. 1.3 for the anode wire voltages used in the experiment. The number of electrons produced in the avalanche is randomly sampled from the corresponding distribution depending on which anode wire section the electron terminated; the number of electrons produced is stored as a number instead of multiple instances of the original electron to save space and computation time. We assume that the lateral movement along the wire arising from $\vec{E} \times \vec{B}$ effect near the wire is negligible as compared with diffusion and other effects described later.

It is worth mentioning there is the possibility to simulate the space charge effects in this class where the inverse to the correction map described in 1.2.8 is applied to the drifting electrons. This is not used for calculating the response of the TPC for efficiency calculations since it is a trivial exercise to input the space charge map and correct for it using the same inverse map.

1.3.2 Pad Response Task

The total charge of each avalanche must be distributed according to the pad response function (PRF) described in section ???. The PRF is simulated as the double integral of a 2-dimensional Gaussian. The final output charge on all the pads are the superposition of the PRFs of all drifted electrons. The MC PRF is expressed as,

$$PRF(x, z) = \iint e^{-\frac{(x-x_0)^2}{2\sigma_x^2}} e^{-\frac{(z-z_0)^2}{2\sigma_z^2}} dx dz, \quad (1.9)$$

where $\sigma_x = 3.4$ and $\sigma_z = 3.5$, and x_0 and z_0 are the final position of the drifted electron. The σ parameters were determined through an iterative comparison matching the PRFs of the MC and experimental data sets. We can see good agreement between the MC PRF for π^- in Figure ??, and the data PRF, Fig. ??, where the black line is the PRF fit to the experimental data. It is sufficient to use such a simple universal PRF function as we can describe all the crossing angle effects discussed in ???. Therefore these effects must arise from geometric effects related to the track angle, the amount of charge distributed over an anode wire, and the superposition of the PRF from neighboring anode wires which contribute to the appearance of a changing PRF.

1.3.3 Electronics Task

The electronics task simulates the electronics response, converting the induced charge on a pad into ADC channels. The conversion from number of electrons to the response, R , in ADC channels is calculated as,

$$R = A_{tot} \cdot e \cdot \frac{ADC_{max} - ADC_{pedestal}}{f_c} \quad (1.10)$$

,

where e is the typical charge of an electron in fC, A_{tot} is the total number of avalanche electrons, $ADC_{pedestal}$ is the pedestal (300 ADC, ADC_{Max} is the maximum allowed ADC value (4096), and

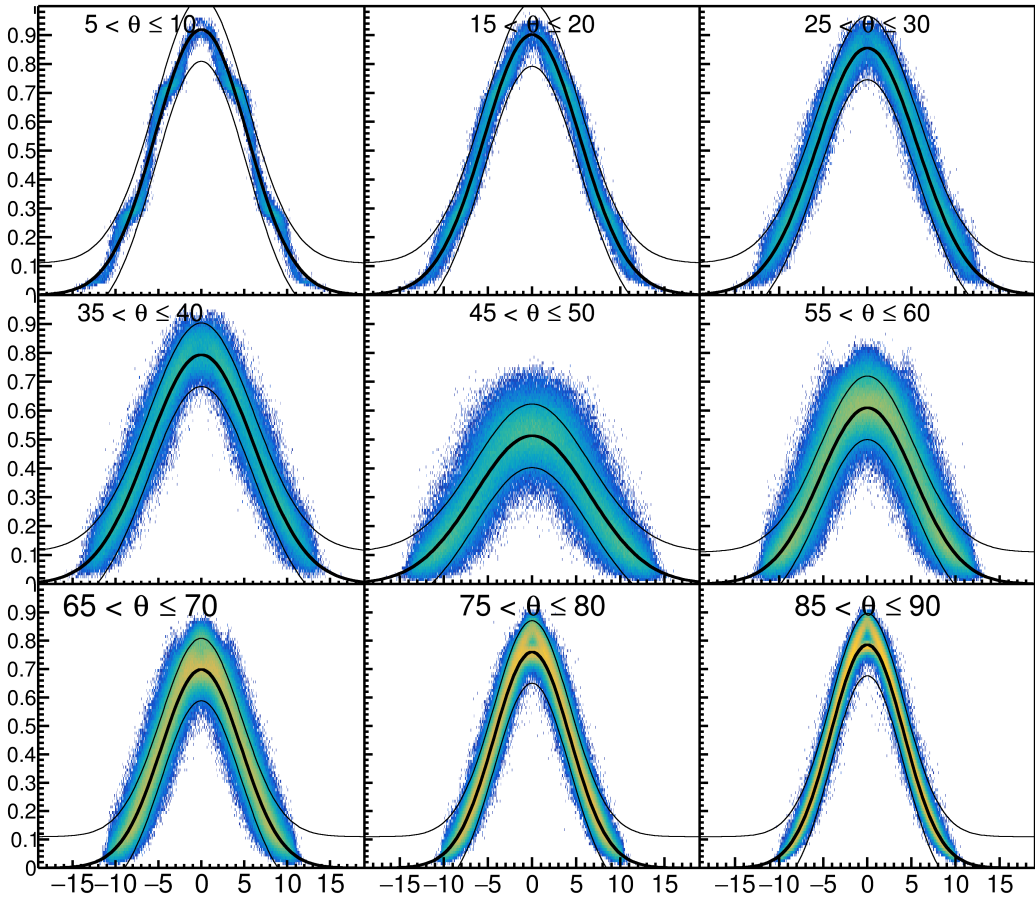


Figure 1.20: PRF response of Monte Carlo simulation of π^-

f_c is the dynamic range setting (120 fC). We add random Gaussian noise as measured from the experimental simulating the electronic noise; (RMS) was measured to be around 6 ADC.

The induced current in the pad goes through a pre-amplifier and shaping amplifier which determine the final pulse shape that is read out. The pulse shape did not change significantly in any circumstance, such as pulse height, data type, or particle type, for a given shaping constant. This allows us to assume the pulse shape is constant with the only two variables being the height of the pulse, Q , and the starting time bucket of the pulse, t_o . The shaping constant was set to 117 ns for the data analyzed here. Figure 1.21 shows the pulse shape experimentally extracted from signals that did not saturate the electronics over a wide range of ADC values; it is normalized so the maximum

height is 1.

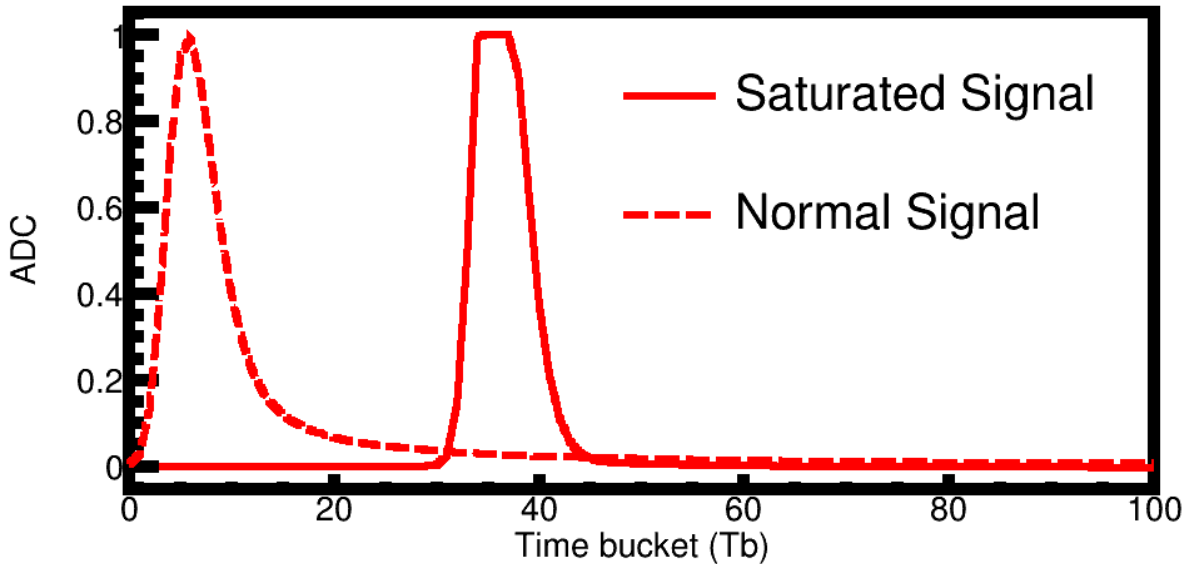


Figure 1.21: Standard pulse

1.3.4 Simulating Saturation

There are several types of saturation that must be simulated or accounted for to correctly model the TPC response. They all are varying degrees of the same effect which manifest in different ways in the detector. In general all amplifiers have a finite range of output values set by a positive and negative rail (typically -12V and +12V). If the input charge into a charge sensitive pre-amplifier causes the output voltage to reach the max (or min) output voltage, the electronics is considered saturated and the response may be non-linear. The picture is complicated by the fact that there is usually an RC feedback loop which dissipates the input charge. The time in which a pre-amplifier returns to its typical linear behavior depends on the input charge and how quickly it can be dissipated [8]. The pad is otherwise considered dead and no further charge can be measured until the electronics recover.

Due to the long high energy tail in energy loss distributions of a particle traversing matter, it is common to see pads along the track which have very high energy loss values and saturate the

electronics of that pad, even for minimum ionizing tracks. Saturation in this case is infrequent and not an issue as many other clusters are not saturated. As the particle's charge gets higher, or the momentum gets lower, the mean energy loss value gets much higher and a significant fraction of pads in a track may be saturated. While earlier we outlined an algorithm to correct the saturation for the track measurement itself, saturation also affects surrounding tracks.

As mentioned earlier the pad is dead for some time, which depends on the total input charge. For charges that are relatively at or above the threshold for saturation the pad is certainly dead for the remainder of time of the measurement; i.e. $T_{dead} > 10 \mu\text{s}$. This will cause signals from other tracks passing underneath the offending track to not be measured; the saturated pad "shadows" any future signal. In the case where two tracks are separated in time due to different polar angles, but have significant overlap in a pad-plane projection, a significant portion of the later track may be shadowed and the track itself will suffer in quality significantly. For events with high track multiplicity this causes a significant shadowing effects, in that the upward going tracks recorded at earlier times shadow the downward going tracks recorded at later times. This will change event by event and is very difficult to simulate except through a MC track embedding approach which will be discussed later.

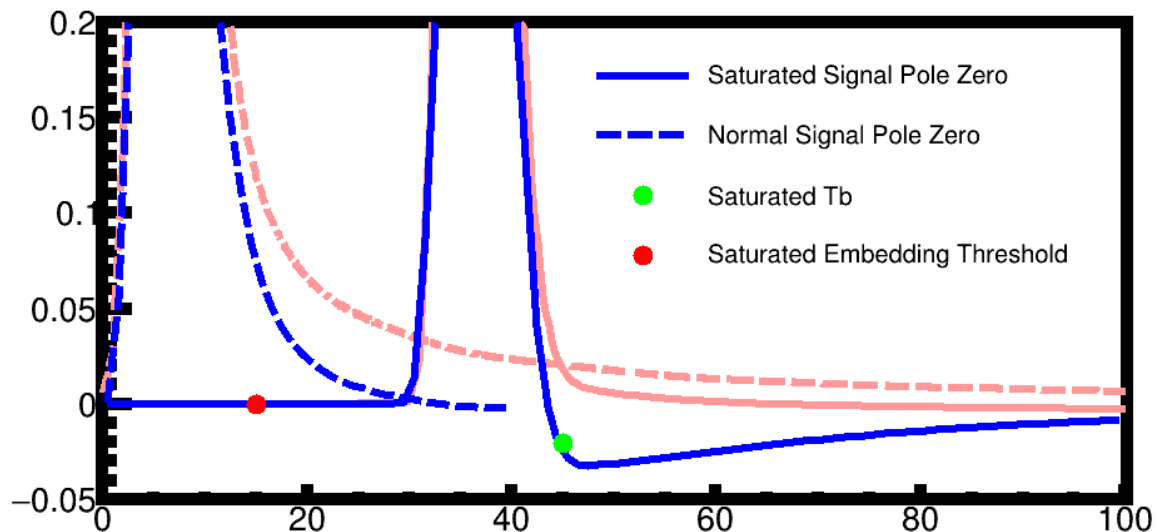


Figure 1.22: Pole zero correction

In the case where the input signal is very large, the electronics can be dead for up to 35 ms [8]. The beam rate in the experiment was about 10 kHz, which corresponds to an average of 10 μ s between subsequent beams. Pads can be effectively dead for several events before recovering. Due to the large charge of the beam, a large amount of very high energy electrons are produced via scattering from the beam passing through the gas. In the presence of the magnetic field the radius of curvature of most of the electrons are within several cm. Figure 1.23 shows the horizontal extent of the electrons in a top down view of the TPC. While some of the electrons can stop in the gas, a significant fraction can travel to the top and bottom of the TPC. These electron can pass through the gating grid without being blocked and either terminate on the pad or possibly deposit their charge directly in the pad. The charge induced on the pad was large enough to kill the pad for a time long enough to last until at least the next event. These pads are dead for the whole event and are randomly distributed around the beam path projection on the pad plane.

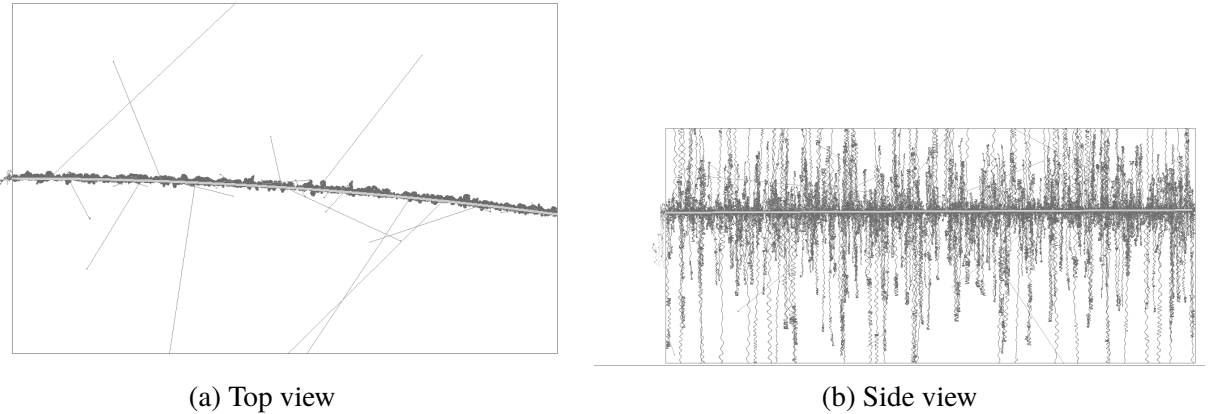


Figure 1.23: Geant4 simulation of ^{108}Sn beam at 270 MeV/A in P10 gas. Notice the extent of the delta electrons in the vertical direction as compared to the horizontal extent.

Simulation of saturation is handled naturally by embedding MC tracks into real data, by correctly identifying when in the time bucket spectrum saturation has occurred in each pad. Once the time of saturation has been identified, no further signals are embedded as the pad is assumed to be dead. In the case a pad is dead for the whole event the time of saturation is set to the first time bucket and no signal is embedded. The characteristic signature of a saturated signal is the fast fall time of the falling edge of the pulse going quickly to zero, as opposed to the long tail of normal pulses as seen

Run 2481, Event 8

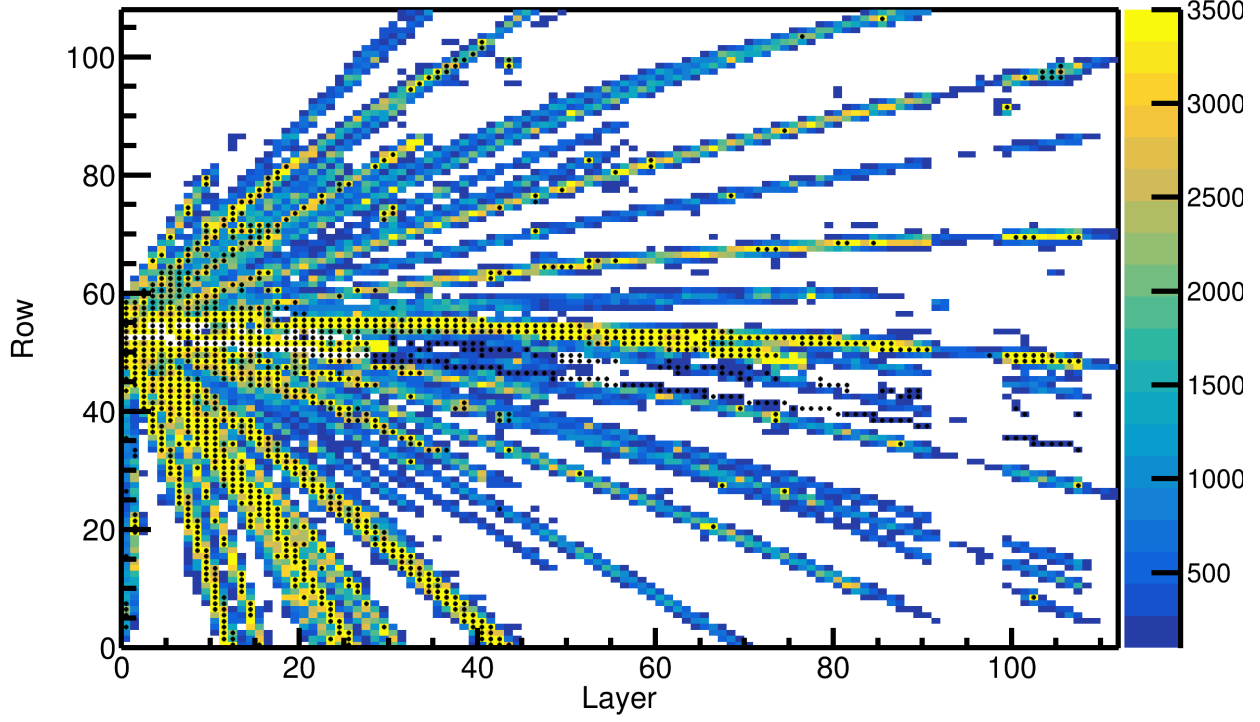


Figure 1.24: Tagging the saturated pads.

in Fig. 1.21. The long exponential tail can be effectively removed by a simple software technique which is similar to the electronics concept of “pole-zero compensation”. If the raw ADC value at a particular time, i , is represented as f_i , the corrected pulse which differentiates out the exponential tail, f'_i can be expressed as,

$$f'_i = \frac{-b_1 \cdot f'_{i-1} + a_o \cdot f_i + a_1 \cdot f_{i-1}}{b_o} \quad (1.11)$$

where $a_o = .9723$, $a_1 = -.9453$, $b_o = .9545$, and $b_1 = -.9203$. These numbers are experimentally fit to give the fastest, non-zero, correction to the tail of a normal pulse. This correction produces a negative undershoot for the saturated pulse, since there was no long exponential tail to begin with. Figure 1.21 shows before the correction technique as the red curves, and after the technique as the blue curves for both the normal and saturated pulse. As the program is looking for and identifying positive peaks in the spectrum, we also calculate the corrected ADC value of that particular time

bucket according to Eq. 1.11. A peak is identified as a saturated signal if it is less than $-20 \cdot G$ for more than 8 Tbs, where G is the gain calibration of the pad, and the max ADC value is $> G \cdot 500$ to eliminate false negative pulses which come from the gating grid subtraction in dead pads. The saturated flag is set to true and the data time bucket position of saturation is set to $t_{peak} - 5$, where t_{peak} is the time bucket of the negative peak. The MC time bucket position is set to $t_{peak} - 30$ to ensure that the MC signals do not overlap the saturating data signal.

Saturation can also occur if the sum of all the pulse heights are over the max ADC threshold of 3500 ADC. This is because the fall time of the pre-amplifier circuit is much longer than the time bucket window and pulses are allowed to pile up. While pads that saturate via this method still are identified through the same algorithm described above, nothing is done in the MC class to take this into account when embedding signals. We assume this method of saturation is a higher order correction and the current algorithm approximates most of the saturation effects. Figure 1.24 shows the tagging algorithm for an event in the TPC. The max ADC values in a given pad are colored and the black dots are pads tagged as saturated. Some pads appear to be below 3500 ADC, but upon further inspection they satisfy the sum of all the signals causes saturation though the max ADC never goes over 3500.

Dead pads are identified earlier in the software in the STCore.cc class. A dead pad is classified as having a r.m.s. value < 50 ADC and a max ADC < 50 . The saturated flag is set to true, and the time bucket position of saturation in both the data and MC are set to the first time bucket.

1.4 Monte Carlo Track Embedding

The TPC monte carlo simulation was built upon Geant4, including the dimensions, materials, and gas composition. Several classes were built to simulate the operations of a Time Projection Chamber (TPC). This included the drift properties of electrons, avalanche process, and electronics response to input signals. Combined, these classes simulate the response of the TPC to any input MC track and can be directly input into the S π RIT TPC software reconstruction algorithm.

While the goal of these tasks are to simulate important properties of a TPC, there are several effects which cannot be easily simulated. Several examples are biases due to triggering detectors (preferential selection of a reaction plane), saturation effects in the electronics, track multiplicity, and several other systematic sources common to all experiments. Simulating each issue individually would be impractical and time consuming, if not impossible. By embedding monte carlo tracks into experimental data – and propagating through the tracking and reconstruction algorithm – one can account for all sources with a monte carlo type approach.

Track embedding is the process of taking a simulated MC track from Geant4 and embedding its response into a real data event. After reconstructing this new embedded event we match the input MC track to its corresponding final reconstructed track. By doing so we can evaluate the response of the entire TPC system to any given input value. The TPC system is composed of three major components, each which can introduce errors and or biases; the software, the detector, and the experimental setup.

As discussed in Section 1.1, the software is composed of several tasks, each introduce biases through assumptions made in the tracking algorithm. The detector system introduces errors related to the physical measurement itself which can be addressed through modeling the TPC, and its materials. The biases involved in the the experimental set up are not always obvious but present in the experimental data. All three of these can be simultaneously addressed by embedding of MC tracks. Before beginning the detailed description of the embedding software, it is worth noting that the MC embedding was analyzed as a separate data set from the published data to avoid any issue of MC embedded tracks making it into the final published data.

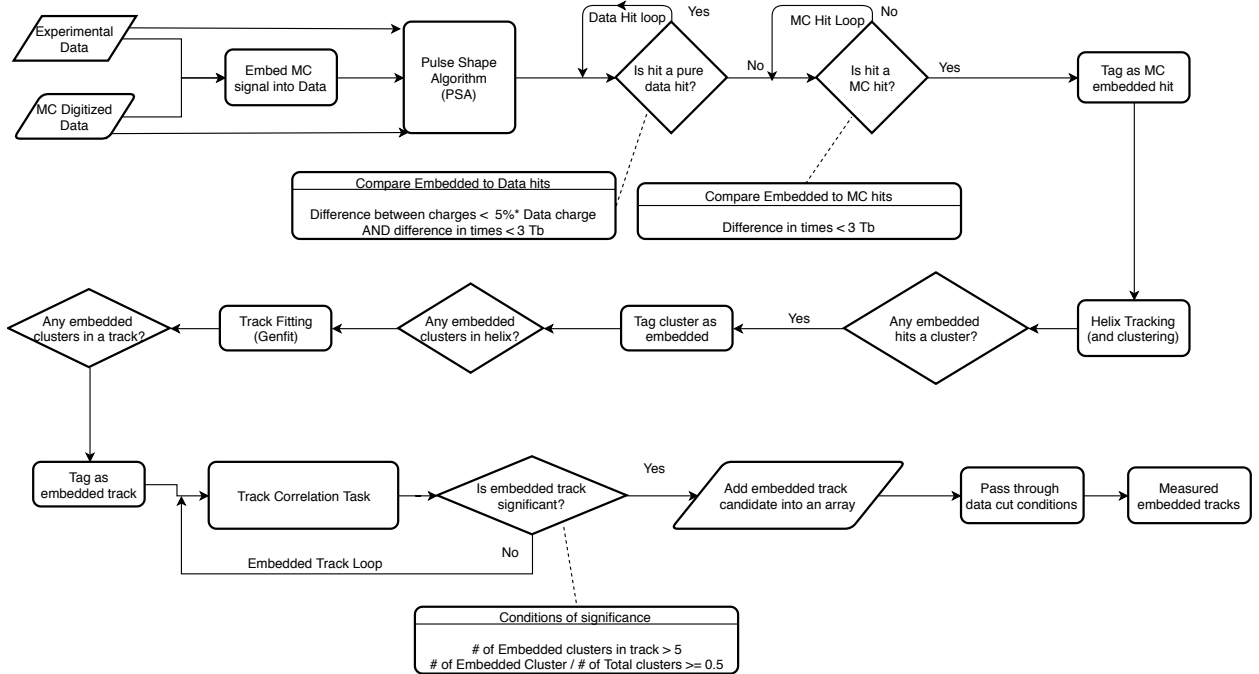


Figure 1.25: Flow of embedding implementation in the software.

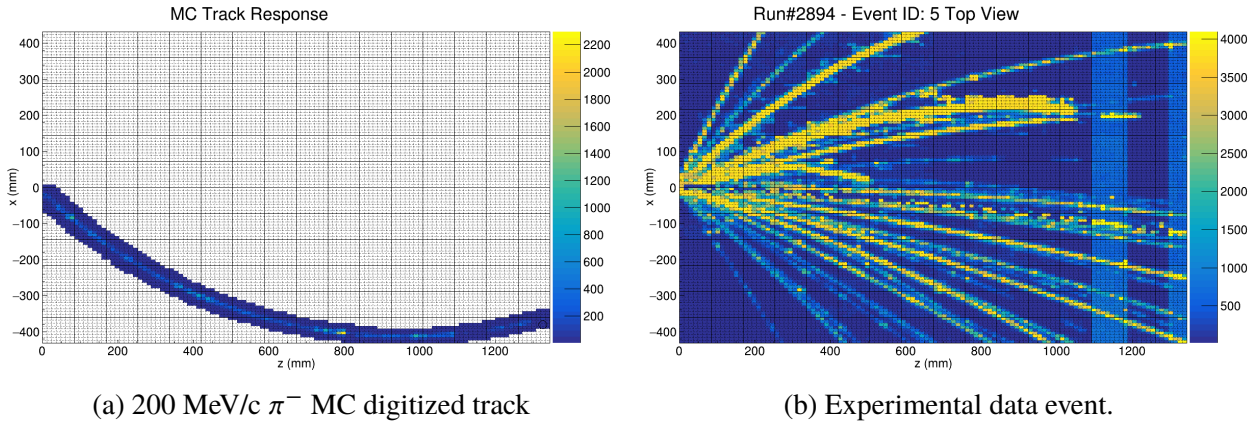


Figure 1.26: A 200 MeV/c π^- embedded into a nuclear collision type event. The embedded track identified by the software is highlighted by the solid green line.

The detailed flow diagram of the software implementation of embedding is shown in Fig. 1.25. Once the MC simulation of a track response in the TPC is created, we directly embed the MC signals into data by superimposing the MC signals into the data time bucket spectrum, pad-by-pad. Figure 1.26a shows the response of a 200 MeV/c π^- track in the TPC; we will embed this track into the data event, Fig. 1.26b, for an example. We will refer to experimental data containing embedded

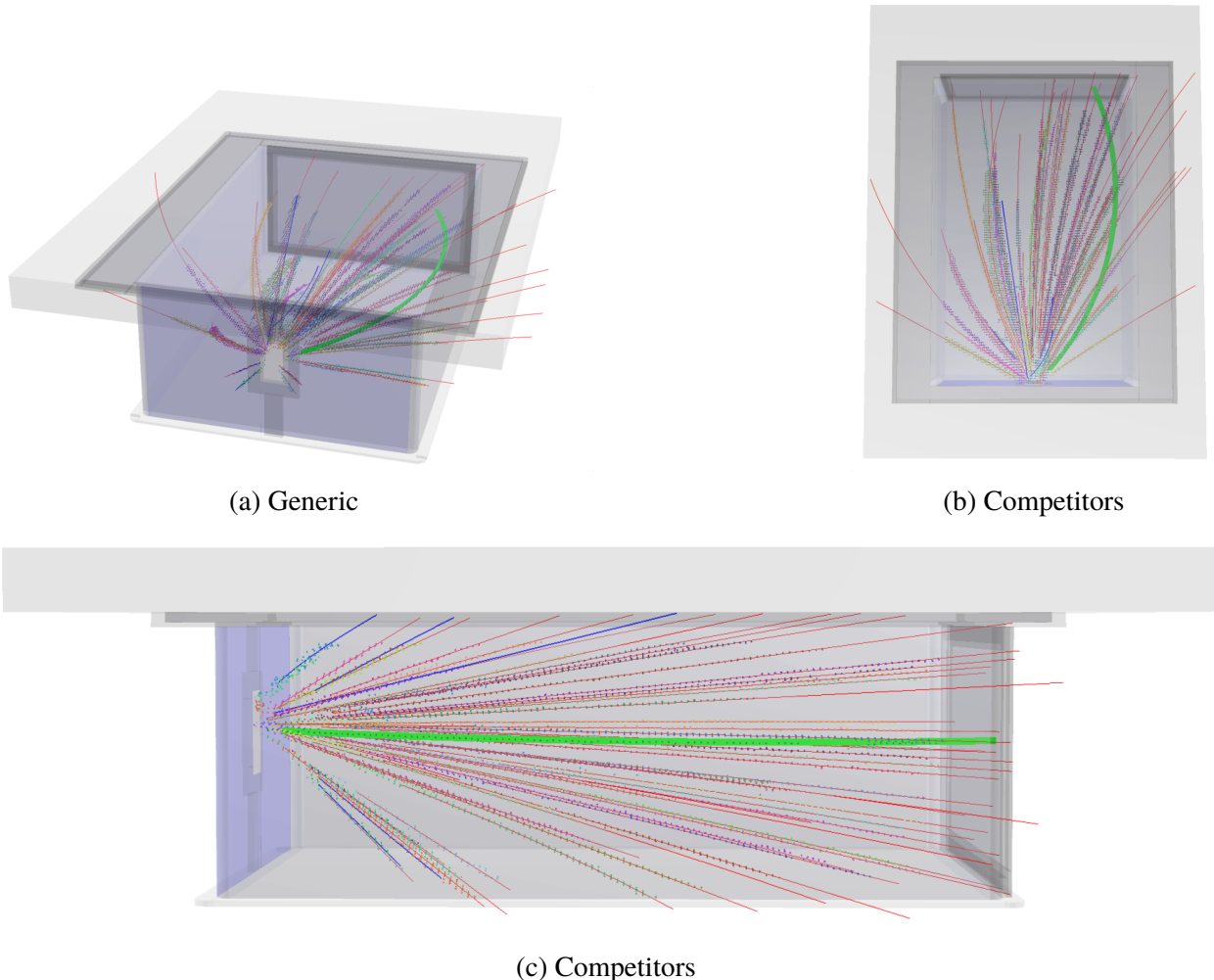


Figure 1.27: A 200 MeV/c π^- embedded into a nuclear collision type event. The embedded track identified by the software is highlighted by the solid green line.

MC signals as “embedded data”, data only containing the MC signals as “MC data”, and data only containing only the experimental signals as “experimental data”. The three set of data are each independently analyzed by the PSA algorithm, Section 1.1.1, which finds all the hits in each data set.

After this, the PSA algorithm contains the first and most important part of the embedding software. Here the PSA task has the job to identify which hits in the embedded data are originally MC hits and which are from the original experimental data. Once identified, the embedded hits can be tagged and tracked through the entire software. By comparing the hits identified in

the embedded set against the experimental data set we can first identify which embedded hits belong to the original experimental hit subset. For hits to match, they must satisfy two criteria, $|Q_{\text{Data}} - Q_{\text{Embed}}|/Q_{\text{Data}} < .05$ and $|t_{\text{Embed}} - t_{\text{Data}}| < 3$ where Q and t represent the charge and time of the hit respectively. We then remove these hits in the embedded data set which satisfy the conditions of experimental data hits.

The surviving hits are then compared with the MC hit data set, where the criteria for a matching MC hit is, $|t_{\text{Embed}} - t_{\text{MC}}| < 3$. We do not require a matching criteria for the charge values since as not to bias the charge values selected as identified MC hits. This is only accomplished by first removing almost all of the experimental hits in the first step. Each embedded hit that passes this criteria is tagged as an MC embedded hit. From here, the embedded data is treated as if it were real data passing through the same software analysis.

The goal of this naïve tagging is to preserve all the information of where the embedded hits, clusters, and tracks have gone. If a helix track has one hit that is embedded it will be tagged as embedded. When the hits in a helix track are clustered, if a cluster contains one embedded hit it is itself tagged as an embedded cluster. Furthermore, if a track that is reconstructed contains any embedded clusters, it is an embedded track. It is the job of the embedded correlation task is to identify which of the final embedded tracks are candidates for the original input track. Several things may happen along the process of embedding. A track could break up, lose or share its charge with an adjacent track, or maybe not be identified at all for a variety of other reasons. For the embedded track to be a candidate of the input MC track, it must satisfy two conditions, $N_{\text{sat}} > 5$ and $N_{\text{sat}}/N_{\text{Total}} \geq .5$, where N_{sat} is the number of saturated clusters in a track and N_{Total} is the number of total clusters. The first criteria is a simple minimum cut where to ensure there exists an embedded track. The second criteria is the strongest cut ensuring the track has at least half of its clusters coming from embedded MC signals. The set of tracks which satisfy both conditions are saved into an array of tracks which the user can use to study efficiency or track splitting.

In the case of efficiency analysis the user must select what they believe to be the track which most represents the original track. In this thesis, the track with the minimum distance to vertex is

identified as the correct track. This is to get rid of the situation of track splitting where typically the split track has a distance to vertex which is very large and cut out from the analysis. The details of how the embedding is used to calculate the efficiency will be described later.

1.4.1 MC and Data Comparison

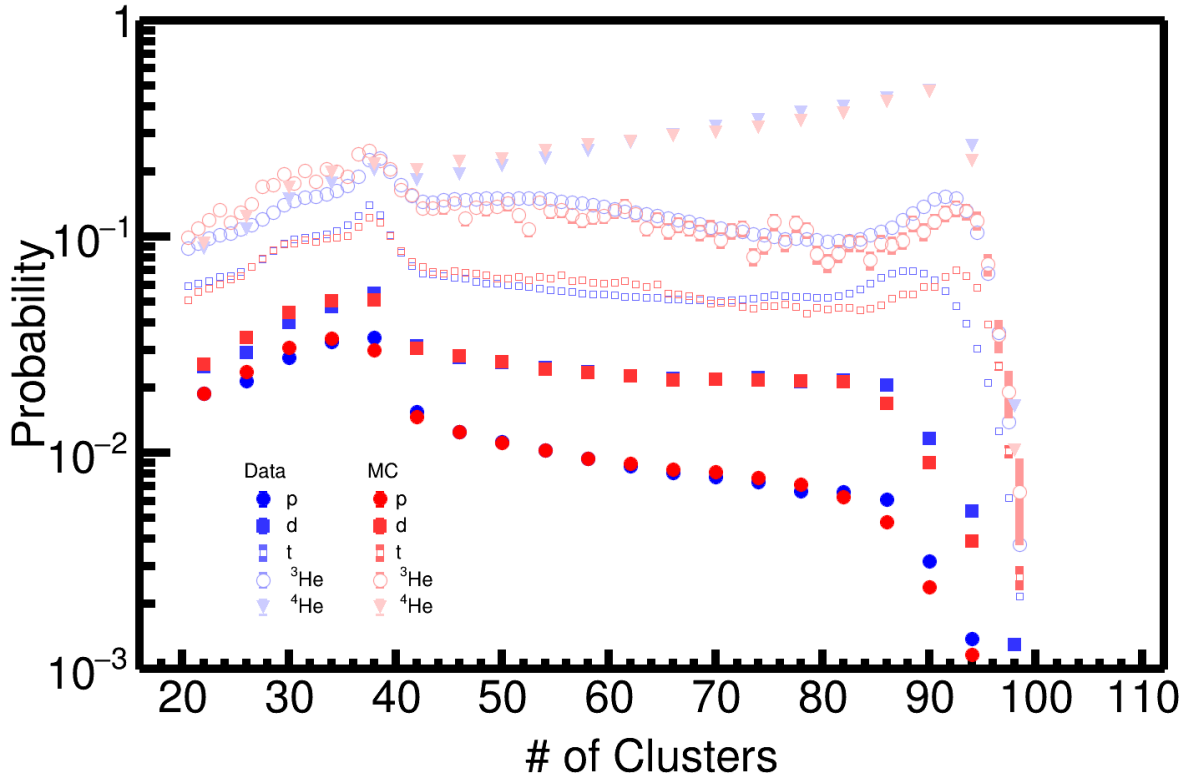


Figure 1.28: Comparison of MC to data.

Add Figure of Pad response function for pion, proton.... for MC vs Data vs angles... Add Figure of Number of clusters of MC vs Data Add Figure of dE/dx MC vs Data Add Figure of Momentum resolution MC vs Data Add Figure of track residuals? MC vs data?

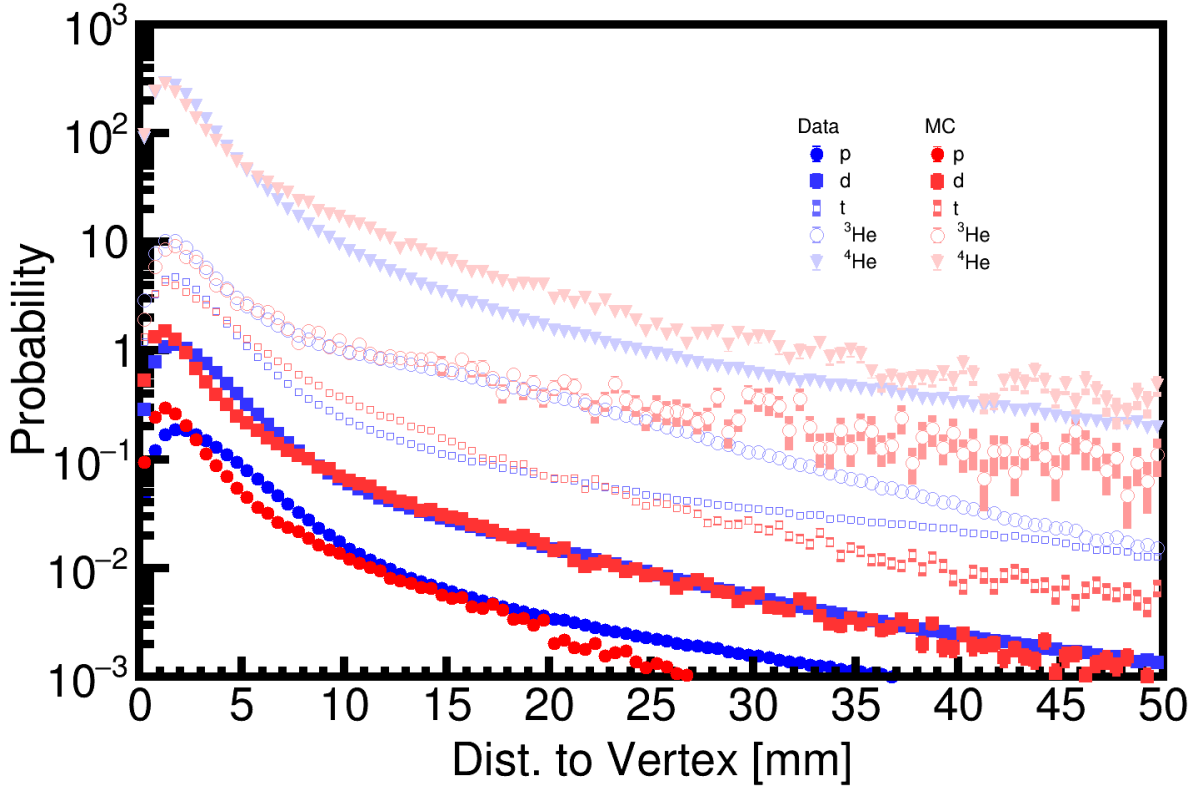


Figure 1.29: Comparison of MC to data.

1.5 Aligning TPC

1.6 CoBo timing correction

The arrival time of signals originating from each pad may differ due to timing delays in the electronics and cabling. The timing differences will affect the y-position measurement of each track. The y-residuals reveal that the timing differences correspond to about ± 2 mm in position differences. The timing difference is stable for each pad across several runs. Figure ?? shows the y-residuals, across all the rows , for three different layers. Before the correction one can see large deviations in the y-residuals which correspond to timing differences. The mean value of the y-residual distribution is fitted and a map is constructed for each pad. The data is then reconstructed subtracting the value of that map, dy , for each pad. The resulting corrected distribution is shown in Fig. ?? for the same layer set. Figure 1.31 also show the summary of all the pads before

the correction and after the correction. There is a significant improvement in the width of the distribution going from 1.5 mm to 0.6 mm.

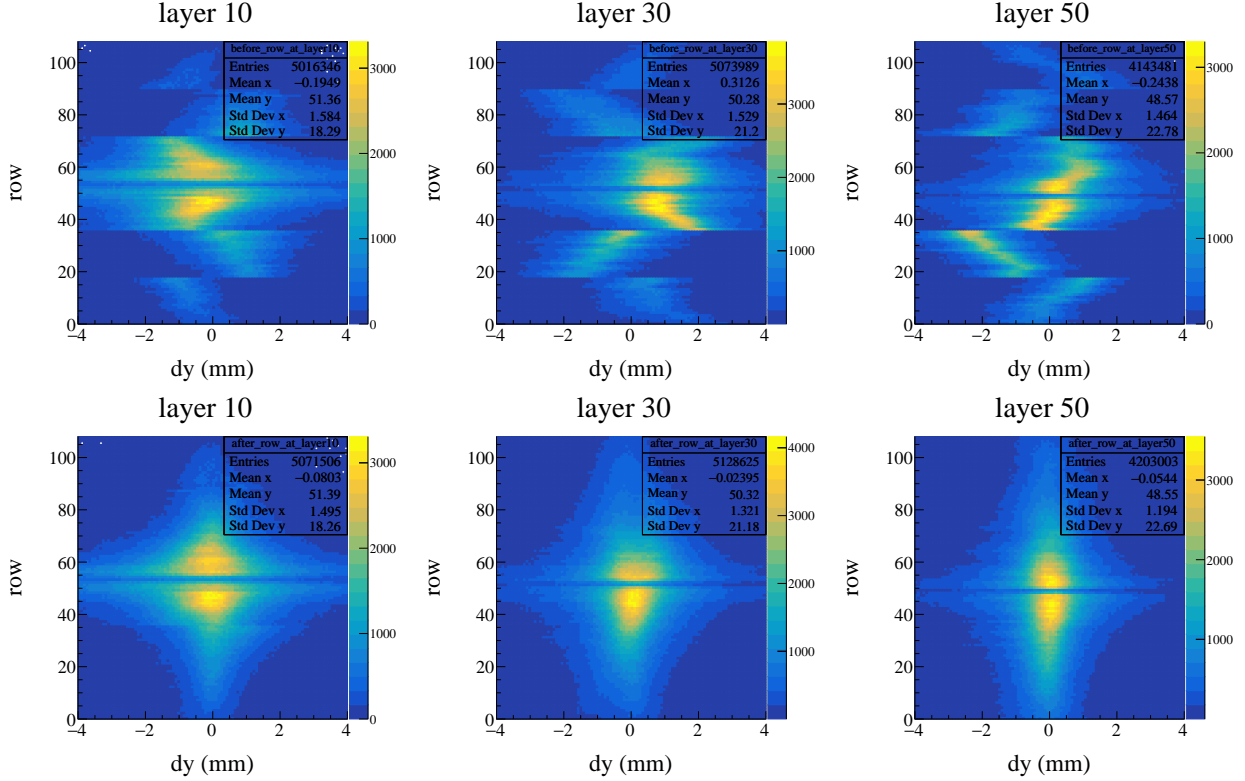


Figure 1.30: TBW

1.7 Efficiency Corrections

Add Figures of efficiency vs angles in TPC polar angle plot for pions

Since the S π RIT TPC is a fixed target experiment it's angular coverage is certainly not 4π . Because the target is several cm away from the widow of the field cage the geometric acceptance is not even 2π . The rectangular design complicates the calculation of the geometric acceptance, or the efficiency.

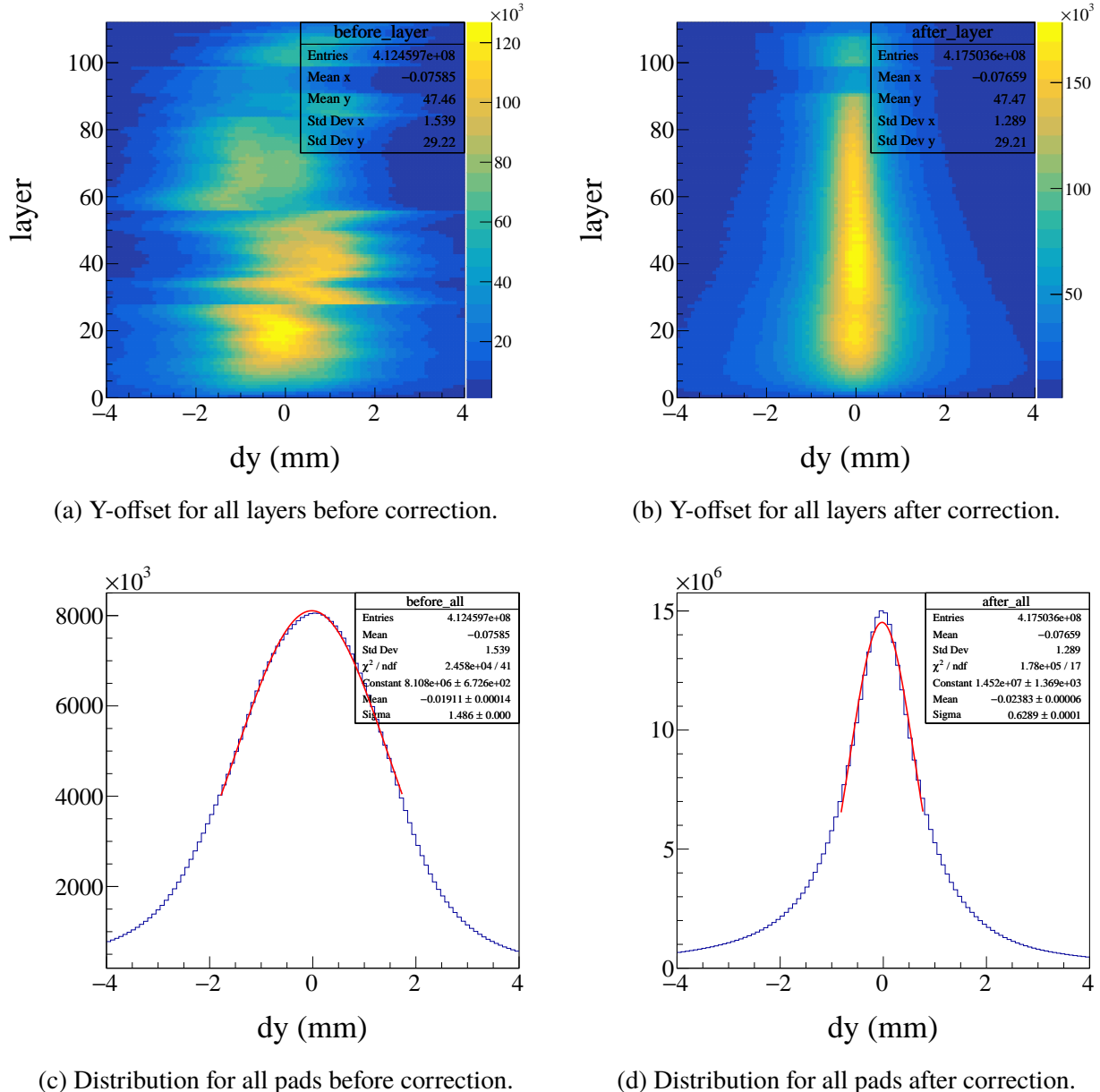


Figure 1.31

APPENDIX

APPENDIX

RUNS ANALYZED IN THIS DATA

System	#runs	Run numbers
$^{132}\text{Sn} + ^{124}\text{Sn}$	113	2841, 2843, 2844, 2845, 2846, 2848, 2849, 2850, 2851, 2852, 2855, 2856, 2857, 2858, 2859, 2860, 2861, 2875, 2877, 2878, 2879, 2880, 2881, 2882, 2883, 2884, 2887, 2888, 2889, 2890, 2891, 2892, 2893, 2894, 2896, 2898, 2899, 2900, 2901, 2902, 2903, 2904, 2905, 2907, 2914, 2916, 2917, 2919, 2920, 2921, 2922, 2924, 2925, 2926, 2927, 2929, 2930, 2931, 2932, 2933, 2934, 2935, 2936, 2939, 2940, 2941, 2942, 2943, 2944, 2945, 2946, 2948, 2955, 2956, 2958, 2959, 2960, 2961, 2962, 2964, 2965, 2966, 2968, 2969, 2970, 2971, 2972, 2973, 2975, 2976, 2977, 2978, 2979, 2980, 2981, 2982, 2983, 2984, 2985, 2986, 2988, 2989, 2990, 2991, 2992, 2993, 2997, 2999, 3000, 3002, 3003, 3007, 3039
$^{124}\text{Sn} + ^{112}\text{Sn}$	60	2542, 2543, 2544, 2546, 2547, 2548, 2552, 2553, 2554, 2555, 2556, 2557, 2558, 2559, 2560, 2562, 2563, 2564, 2565, 2566, 2567, 2568, 2569, 2570, 2571, 2572, 2573, 2574, 2575, 2578, 2579, 2580, 2581, 2582, 2583, 2584, 2585, 2586, 2587, 2588, 2589, 2590, 2591, 2592, 2593, 2594, 2595, 2596, 2597, 2598, 2599, 2600, 2601, 2617, 2618, 2619, 2620, 2621, 2622, 2623
$^{112}\text{Sn} + ^{124}\text{Sn}$	68	3059, 3061, 3062, 3065, 3066, 3068, 3069, 3071, 3074, 3075, 3076, 3077, 3078, 3080, 3081, 3082, 3083, 3084, 3085, 3087, 3088, 3089, 3090, 3091, 3092, 3093, 3094, 3095, 3097, 3098, 3102, 3103, 3138, 3139, 3140, 3141, 3142, 3143, 3144, 3145, 3146, 3148, 3149, 3150, 3151, 3152, 3153, 3154, 3155, 3156, 3157, 3158, 3159, 3165, 3166, 3167, 3168, 3169, 3170, 3171, 3172, 3177, 3179, 3180, 3181, 3182, 3183, 3184
$^{108}\text{Sn} + ^{112}\text{Sn}$	85	2272, 2273, 2274, 2275, 2276, 2283, 2284, 2285, 2286, 2288, 2289, 2291, 2310, 2311, 2314, 2315, 2320, 2322, 2323, 2324, 2325, 2331, 2332, 2333, 2334, 2335, 2336, 2337, 2340, 2341, 2362, 2363, 2368, 2369, 2370, 2371, 2372, 2373, 2374, 2375, 2378, 2379, 2380, 2381, 2382, 2383, 2384, 2385, 2386, 2387, 2388, 2389, 2391, 2392, 2393, 2394, 2395, 2396, 2397, 2398, 2399, 2400, 2401, 2402, 2429, 2432, 2433, 2434, 2437, 2438, 2439, 2440, 2442, 2453, 2461, 2462, 2463, 2501, 2502, 2503, 2505, 2506, 2507, 2508, 2509

Table .1: List of runs for the analysis.

APPENDIX

SECOND APPENDIX

BIBLIOGRAPHY

BIBLIOGRAPHY

- [1] M. Al-Turany, et al., The fairroot framework, *J. Phys.: Conf. Ser.* 396 (2). doi:10.1088/1742-6596/396/2/022001.
- [2] C. Höppner, et al., A novel generic framework for track fitting in complex detector systems, *Nucl. Instrum. Meth. A* 620 (2-3) (2010) 518–525. doi:10.1016/j.nima.2010.03.136.
- [3] W. Waltenberger, Rave—a detector-independent toolkit to reconstruct vertices, *IEEE Transactions on Nuclear Science* 58 (2) (2011) 434–444. doi:10.1109/TNS.2011.2119492.
- [4] H. Bichsel, A method to improve tracking and particle identification in tpcs and silicon detectors, *Nuclear Instruments and Methods in Physics Research Section A: Accelerators, Spectrometers, Detectors and Associated Equipment* 562 (2006) 154–197.
- [5] E. Gatti, et al., Optimum geometry for strip cathodes or grids in mwpc for avalanche localization along the anode wires, *Nucl. Instr. Meth. Phys. Res. A* 163 (1979) 83–92. doi:10.1016/0029-554X(79)90035-1.
- [6] S. Collaboraiton, Samurai dipole magnet field map (2020).
URL <https://ribf.riken.jp/SAMURAI/index.php?Magnet>
- [7] G. Van Buren, et al., Correcting for distortions due to ionization in the star tpc, *Nucl. Instrum. Meth. A* 566 (1) (2006) 22–25. doi:10.1016/j.nima.2006.05.131.
- [8] T. Isobe, et al., Application of the generic electronics for time projection chamber (get) readout system for heavy radioactive isotope collision experiments, *Nucl. Instrum. Meth. A* 899 (2018) 43–48. doi:10.1016/j.nima.2018.05.022.